REV.	BY & DATE	DESCRIPTION	CHECK	APPROVED & DATE
Prepared William McClintock, Eric Bradley, and Gregory Holsclaw	June 1, 2004	On-ground calibration report for the MASCS instrument.		

ADVISORY: This document has NOT been reviewed for export control and therefore may be subject to ITAR regulations or requirements.

Ralph L. McNutt, Jr., Project Scientist — Date 7/27/04

Robert Gold, Payload Manager — Date 7/27/04

Noam Izenberg, Instrument Scientist — Date 8/9/04

William McClintock, Cognizant Co-I — Date 7-28-04

Mark Lankton, Instrument Engineer — Date 7/27/04

Released — Date

PART NUMBER	SIZE	NEXT ASSEMBLY	QTY./NA	USED ON	EFFECTIVITY - END ITEM SER. NO.	WEIGHT

THE JOHNS HOPKINS UNIVERSITY
APPLIED PHYSICS LABORATORY
11100 JOHNS HOPKINS ROAD, LAUREL, MARYLAND 20723-6099

MESSENGER Mercury Atmosphere and Surface Spectrometers (MASCS) Calibration Report

	FSCM NO.	SIZE	DRAWING NO.	REV.
	88898	A	7384-9470	A
	SCALE NONE	DO NOT SCALE PRINT		SHEET 1 OF 49

INSTRUMENT CALIBRATION REPORT

Mercury Atmospheric and Surface Composition Spectrometer
(MASCS)
on the
MErcury: Surface, Space Environment, Geochemistry, Ranging
(MESSENGER)
Mission

LASP/CU Document Number: 20580-T6-XXXX

FSCM NO.	SIZE	DRAWING NO.	REV.
88898	A	7384-9470	A
SCALE	DO NOT SCALE PRINT	SHEET 2 of 49	

Table of Contents

1.0 INTRODUCTION

The Mercury Atmospheric and Surface Composition Spectrometer (MASCS) is one of seven science instruments aboard the MErcury: Surface, Space ENvironment GEochemistry and Ranging (MESSENGER) spacecraft. It is designed to provide measurements that address four of the six science questions that frame the MESSNEGER mission.

1. What planetary formation processes lead to the high metal/silicate ratio in Mercury?
2. What is the geological history of Mercury?
3. What are the radar reflective materials at Mercury's poles?
4. What are the important volatile species and their sources and sinks on and near Mercury?

MASCS consists of a small Cassegrain telescope that simultaneously feeds a Visible and InfraRed Spectrograph (VIRS) and an UltraViolet and Visible Spectrometer (UVVS). It will obtain maps of surface reflectance spectra of the surface in the 0.115 – 1.45 μm wavelength range that will be used to investigate the mineralogical composition of the surface on spatial scales of 5 km or less. UVVS will measure altitude profiles of known species in order to determine composition and structure of the atmosphere and its variability. It will also search for atmospheric signatures of possible volatile polar deposits and previously undetected atmospheric constituents.

MASCS measurement performance requirements and the characterizations and calibrations required to meet those requirements are documented in the MASCS Instrument Calibration Plan (MICP-LASP/CU Document Number 20580-T6-1106 and APL Document Number 7384-9461a). This report summarized the results from preflight characterizations and calibrations that appear in the MICP. The various measurements were performed at the Laboratory for Atmospheric and Space Physics and at the Applied Physics Laboratory in conjunction with the MASCS environmental qualification testing. They include telescope performance (boresight, spectrometer field of view, telescope off axis response), spectrometer spectral performance (spectrometer wavelength scale, spectrometer point spread function, spectrometer scattered light, and polarization), radiometric sensitivity, and detector characteristics.

2.0 SCIENCE OBJECTIVES

The atmosphere of Mercury is a surface-boundary exosphere, which acts as an interface between the surface and external stimuli impinging upon it. Its composition and behavior are controlled by its interactions with the magnetosphere and the surface. The MESSENGER atmospheric science investigation is based upon four key questions related to the nature of the atmosphere and its relationship to the external processes that modify the surface:

1. What is the composition, structure and temporal behavior of the atmosphere?
2. What are the processes that generate and maintain the atmosphere?
3. What is the relationship between atmospheric and surface composition?
4. Are there polar deposits of volatile material and how are the accumulation of these deposits related to atmospheric processes?

1. What is the composition, structure, and temporal behavior of the atmosphere?

The atmosphere of Mercury is known to contain 6 elements (H, He, O, Na, Ca, and K) which taken together have a surface density at the sub-Solar point of approximately 10^4 atoms cm^{-3} (Hunten et al. 1988). Ground based studies of Na indicate that the atmosphere is spatially and temporally variable. There are orderly changes in Na surface density that are related to changes in solar radiation pressure (Killen et al. 1990). But there are also chaotic variations in the atmosphere. The subsolar Na density has been observed to change by a factor of two on time scales of less than a week and bright Na emission spots have been observed at high northern latitudes and over the Caloris basin.

Our inventory of Mercury's atmospheric composition is incomplete. Current understanding of the source processes (see below) suggest the presence of yet undetected species including Ar, Si, Al, Mg, Fe, S, and OH (from impact vaporization of H_2O). With the exception of Ar, all of the species listed above have strong ground state emission lines (predicted intensities in the range 10 Rayleighs - 1000 Rayleighs, e.g. Morgan and Killen 1996) in the spectral range 130 – 600 nm. To date, observational constraints have prevented us from detecting these species from the ground or from earth-orbiting spacecraft.

The measurements required to support the investigation of Mercury's atmospheric composition and structure are: 1) altitude profiles of known species (H, O, Na, and K) measured with a vertical resolution comparable to an atmospheric scale height (25 - 50 km) and a latitude/longitude resolution of 10 - 20 ˚, and 2) a sensitive search for predicted species which have not been previously observed (Si, Al, Mg, Fe, S, OH, etc.).

The UVVS channel of MASCS is specifically designed to make these measurements. It provides broad spectral coverage (115 - 600 nm), moderate spectral resolution (1 nm), and high sensitivity (detection limits ~ 100 Rayleigh), enabling it to produce a detailed inventory of the species in the atmosphere of Mercury (or strong upper limits) together with the vertical and horizontal distributions of the most abundant species. In addition to determining composition and structure, these data will provide the basis for determining atmospheric processes, studying the relationship between surface and atmospheric composition, and studying surface-atmosphere-magnetosphere interactions.

2. What are the processes that generate and maintain the atmosphere?

The processes that supply and remove atmospheric material are identified but their relative importance poorly understood. Hydrogen and helium are likely derived from neutralized solar wind ions, although photodissicoation of meteoritic water and crustal outgassing should supply a portion of these two species, respectively. Proposed sources for Na, K, and O include impact vaporization, ion sputtering, photon stimulated desorption, thermal desorption, and crustal degassing. Currently, there is strong disagreement about the relative importance of these four mechanisms (McGrath et al. 1986, Sprague 1990, Morgan and Killen 1996). Determining a comprehensive inventory of atmospheric species and measuring their spatial and temporal distributions will allow us to quantify the dominant sources mechanisms for the various atmospheric species.

The principal loss mechanisms are thermal escape and photoionization with subsequent loss through transport along open magnetic field lines. Although thermal escape appears to be the dominant loss mechanism for both hydrogen and helium, it is probably unimportant for Na and K (Hunten et al. 1988). Photoionization rates for Na and K are relatively well known; however, the total loss rates from the atmosphere are uncertain by a factor of ten because the efficiency with which ions are swept away by the convection electric field. Based on lunar studies (Mendillo et al. 1993), gas-surface interactions may also be an important sink for sodium and potassium.

UVVS measurements of composition and structure will provide the data required to determine atmospheric processes. Distributions for sodium and other species with strong emission lines will permit a definitive determination of their surface interaction. By understanding the interactions of the major species with the surface we can use the inventory to determine the relative importance of the key source processes.

Correlating UVVS data with Energetic Particle and Plasma Spectrometer (EPPS) and magnetometer data will provide an additional tool for understanding atmospheric processes. The magnetic field controls the location and strength of sputtering ion flux as well as the efficiency of photo-ion loss from the planet. By relating local variations in atmospheric composition with the loci of charged particle precipitation on the surface, we can isolate sputtering as a source. Similarly, production rates from impact vaporization, which depend on the magnitude of impact velocity, should peak in the ram direction of Mercury's orbital motion.

We can also examine the importance of crustal outgassing and search for surface features (e.g. the Caloris Basin, Sprague 1990), which are associated with enhanced concentrations of atmospheric sodium or potassium. Establishing a convincing atmosphere-basin correlation requires that we remove the contributions from all other effects, most of which are related to the magnetosphere, the solar wind, and changes in solar UV and EUV flux.

In addition to neutral species, the UVVS should detect prominent ions like Ca+ and Mg^+ along lines of sight, which pass over the poles and extend along the magnetotail. Strong resonance lines for the S^+, Si^+ and Al^+ also fall in the spectral range of the UVVS. A measurement of an element in the atmosphere and the corresponding ion in the tail, will help us determine the rate at which ions are permanently lost from the planet.

3. What is the relationship between atmospheric and surface composition?

Except for the noble gases, hydrogen, and a few volatile species such as sulfur, which are abundant in the micrometeoroid population, species found in the atmosphere are thought to be derived from the regolith and crust. If we can quantify the sources, sinks and the gas-surface interactions of the atmosphere, then measuring other regolith derived elements (Ca, Mg, Al, Fe), will allow us to estimate the relative abundances of these species on the surface. For example, Morgan and Killen (1996) have shown that if sputtering is the dominant source, then the relative abundances of Ca, Al, Fe, Mg, and Si in the atmosphere are related to surface composition.

Atmospheric detection together with detection by the Gamma-Ray and Neutron Spectrometer and by color imaging and surface reflectance spectroscopy, provide the data required to support the correlation between atmospheric and surface composition.

4. Are there polar deposits of volatile material and how are the accumulation of these deposits related to atmospheric processes?

One of the most exciting new discoveries about Mercury comes from ground-based radar backscatter measurements that have been interpreted as arising from polar deposits of water ice on the surface or at shallow depths (Slade et al. 1992, Butler et al. 1993). An alternative interpretation has been offered by Sprague et al. (1996), who conclude that the observations result from deposits of elemental sulfur. In either case, one mechanism that may explain the accumulation of volatile species at the poles is impact vaporization of infalling material followed by atmospheric transport to the poles and trapping in permanent shadows.

The UVVS will search for the presence of water ice deposits at the poles by measuring the distribution of the daughter product of water dissociation, the hydroxyl molecule (OH). Impact vaporization, sublimation, and degassing are expected to contribute water to the atmosphere where photodissociation by sunlight produces OH. Similar source mechanisms will also supply sulfur to the atmosphere. Killen et al. (1995) have calculated the expected atmospheric concentration of OH from both buried and exposed ice deposits for a wide variety of surface conditions. They conclude that the OH surface density should exceed 10^3 cm^{-3} and that the OH emission rate at λ=306 nm should be grater than 100 Rayleighs if the surface temperature is greater than about 110° K. This intensity is easily detectable by the UVVS. Similar calculations for the sublimation and degassing rates for sulfur have not yet been completed; nonetheless, we expect that a surface density of 8 x 10^3 cm^{-3} would produce an emission strength of about 200 Rayleighs at λ=181.3 nm, which would also be easily detected by the UVVS.

Specifically, the MASCS atmosphere measurement objectives are to provide atmospheric composition over the polar regions and to make spectral measurements of atmospheric composition and density as functions of latitude, time of solar day, and time of solar year.

The MASCS will provide data to address MESSENGER science questions regarding the formation process of Mercury and its geological history:

1. What is the extent of mineralogical variation across the surface and across time?
2. What is the rate of space weathering on Mercury and how does it affect spectral interpretations?

1. What is the extent of mineralogical variation across the surface and across time?

The mineralogical composition of Mercury's surface is largely unknown. Although Earth-based observations indicate that the reflectance spectra of Mercury show similarity in shape and slope with those of the lunar highlands, it was recognized that the spectra of the two bodies also show a marked difference. Whereas the Moon's spectrum shows an absorption band near 1.0 μm caused by ferrous iron in pyroxenes and olivines (Adams and McCord, 1970), the Mercurian spectrum shows, at most, a weak feature centered at 0.9 μm in one observation. Intensive efforts to confirm this observation have not been successful and evidence is accumulating that Mercury's surface is low in ferrous iron Fe^{2+} (Vilas,

1985), limiting the average FeO content to less than about 3-6 wt% (Blewett et al., 1997). Clementine UV-VIS multispectral measurements have led to the identification of large regions on the lunar farside that are extremely low in FeO (<3wt%) (Lucey et al., 1998, 2000a). Such areas are believed to be composed of >90% plagioclase feldspar. Furthermore, recent observations of the moon have revealed small areas of the nearside that lack the otherwise ubiquitous 1μm ferrous iron absorption band (Blewett et al., 2002 and references therein), leading to the conclusion that Mercury's surface composition can be classified as pure anorthosite. In addition to anorthosite, there are other possible mineralogies for Mercury with featureless reflectance spectra. Burbine et al. (2002) investigated the spectral properties of aubrite meteorites (enstatite achondrites) and the minerals found in them. They concluded that a Mercurian surface composed of enstatite-rich basalt would have an absorption feature below 0.6 μm caused by sulfur or sulfides, although the survival of these species in the harsh thermal environment at Mercury is unlikely. Earth-based mid-infrared observations show emission features consistent with the presence of both calcic plagioclase feldspar containing some sodium and very-low-FeO pyroxene (Sprague et al. 2002).

The current paradigm for Mercury, derived from earth-based observations, suggests a primary crust composed predominantly of plagioclase feldspar (anorthitic to albitic) with little basaltic materials, showing virtually no large-scale compositional variation. This in contrast to Mariner 10 color data, which reveal the presence of several broad-scale units thought to be enriched in opaque minerals (relatively low albedo and blue color) (Rava and Hapke, 1987;Robinson and Lucey 1997, 2001). Typically, these deposits are observed to have diffuse boundaries and are insensitive to topographic undulations, leading to the interpretation that they may have been emplaced during large-scale explosive eruptions. The Mercurian surface may contain as much as 5-20% meteoritic components that can provide non-typical constituents, like sulfur or carbon. Spectral information obtained in the range 0.4-1.5 μm (reflectance) can identify mineral abundances. Based on results from Clementine lunar observations (Lucey, 2004) the anticipated accuracy should be on the order of 10% or better. Spectral information provided by MASCS can identify not only the major mineralogical components but also determine bulk FeO and TiO_2 using the methods of Lucy et al. (1998, 2000a, 2000b) as well as potential pyroclastic materials. Mariner 10 images also show regions with albedo differences that may indicate a small increase in mafic minerals. Detection of these materials puts important constraints on the formation models of the planet.

Mariner 10 color images show that, despite the heavily agglutinized nature of the surface, many color differences exist that must be due to compositional rather than maturity differences. These units fall into three broad categories: first is the average Mercury composed predominantly of the ancient heavily cratered terrain (intercrater plains). Second, there is a relatively low albedo and blue material that generally appears insensitive to local topographic undulations and exhibits feathered or indistinct margins. This material is possibly relatively rich in opaque mineral content and emplaced in explosive eruptions (Robinson and Lucey, 1997). Interestingly, several smooth plains units appear to be emplaced on top of this unit. The color properties of the smooth plains are similar to the global average - boundaries are visible because the smooth plains embay (lie on top of) this material. Detailed spectral characterization of the smooth plains is a high priority for MASCS. Determining compositional variations within and between smooth plains deposits will give the best chance of understanding the evolution of the crust and the composition of Mercury's mantle (Robinson and Taylor, 2001). One of the more mysterious units seen in the Mariner 10 color images is a class of materials exhibiting high

albedo and red color. These materials were noted in early papers as anomalous high albedo patches in the floors of several craters (Dzurisin, 1977). Similar to the Tycho crater on the Moon, a low albedo annulus is present around the crater Basho.

2. What is the rate of space weathering on Mercury and how does it affect spectral interpretation?

A serious obstacle to the interpretation of any spectral data for Mercury is the intense space weathering environment at Mercury's orbit, which results in a high percentage of the surface being converted to agglutinates or glass (Cintala, 1982). Agglutinates tend to shift band centers, but more importantly suppress band depths, thus making the identification of iron bands difficult – especially with FeO contents below 10wt%. To overcome this problem a key MESSENGER strategy is the acquisition of spectra of as many Kuiperian (immature) ejecta blankets as possible. When an impact crater is formed material from depth is excavated and deposited near the rim – initially, this material is nearly agglutinate free, but over time the space weathering process continually converts crystalline material to aglutinitic material, thus lowering the albedo, reddening the spectral slope and suppressing absorption bands. Even if the true mineralogic properties of fully mature material cannot be recovered, the fresh ejecta blankets will provide a random sample of the local bulk composition. Lucey (2004) has followed such a strategy for the Moon from Clementine spectral data to produce an interpolated 1-km pixel major mineralogy map of the Moon (clinopyroxene, orthopyroxene, olivine, plagioclase feldspar).

Specifically, the MASCS surface composition science measurement objectives are to provide spectral measurement of the surface mineralogy associated with Fe-bearing, Ti-bearing, and other units via visible and near-IR absorption bands.

3.0 DESIGN CONSIDERATIONS

Table 3.1 MASCS Measurement Requirements

	Atmospheric Composition	Surface Compostion
Wavelength Range	115 - 600 nm	0.115 - 1.45 μ
Spectral Resolution	0.6 nm	5 nm
Spatial Resolution	25 km height on limb 15 - 20 ˚ latitude/longitude	< 500 μ radians (< 20 NAC pixels)
Sensitivity	Detection of 10 Rayleigh in 100 sec; 130 < λ < 425 nm	Signal-to-noise > 100

MASCS instrument measurement requirements are summarized in Table 3.1. In general the MESSENGER mission design and launch vehicle selection severely limit both payload mass and data downlink volume. These considerations lead to a design for an atmospheric experiment that employs photomultiplier tubes rather than one using fixed gratings and multi-element detectors. The primary science objectives require a small, low-mass instrument with moderate resolution and very high sensitivity, which can measure a small number (10 – 20) of isolated emissions at known wavelengths spread over a very broad range (115 – 600 nm). (Noble gasses were excluded from the atmosphere measurement objectives because their resonance lines lie in the extreme ultraviolet (< 100 nm), requiring a separate optical train.) Instruments with multi-element detectors require separate optical channels or complicated mechanical devices to switch detectors to meet these wavelength requirements.

Furthermore, when the spectrum consists of a few isolated features, the scanning design has a sensitivity advantage because it has very large light gathering power per spectral resolution element. While fixed grating, multi-element detector designs have a sensitivity advantage where continuous spectral coverage is desired, the argument that they are more likely to discover unsuspected species applies to fly-by missions where observation time is limited. Assuming the spacecraft will orbit Mercury once every 12 hours, thus the UVVS will have adequate time to make a very thorough search for unsuspected emissions over its entire spectral range. Downlink limitations also lead to a point spectrograph rather than a mapping spectrograph design for surface composition studies. Obtaining visible and infrared spectra on a fixed latitude and longitude grid of 5 to 10 km instead of over a continuous swath will provide context for the full coverage color images obtained with Mercury Dual Imaging System (MDIS). Mercury thermal infrared emission limits the spectral coverage for reflectance spectroscopy to < 1.5 microns which is still adequate to measure signatures of ferrous oxide near 1 micron.

4.0 INSTRUMENT DESCRIPTION

The MASCS instrument consists of a well-baffled telescope simultaneously feeding both an Ultraviolet-Visible Spectrometer (UVVS) and a Visible-Infrared Spectrograph (VIRS). The telescope-UVVS configuration is nearly identical to the Galileo UltraViolet Spectrometer (Hord *et al.* 1992). It is optimized for measuring the composition and structure of the atmosphere and for measuring ultraviolet ($\lambda < 300$ nm) surface reflectance. VIRS is mounted on top of the UVVS and is coupled to the telescope focal plane with a short fiber optics bundle. It is optimized for measuring visible and near infrared ($0.3 \leq \lambda \leq 1.45$ μ) surface reflectance.

The MASCS uses a microprocessor-field programmable gate array (FPGA) based logic system to manage instrument configuration, control spectral scanning, and provide spacecraft-instrument communications via an RS-422/RS-232 compatible universal asynchronous receiver transmitter (UART).

The UVVS will measure altitude profiles of known species (H, O, Na, K, and Ca), which will be used to determine atmospheric temperature and density and to map the extended distributions of these species. We will make observations both at a series of fixed wavelengths to search for predicted species, which have not been previously detected (Si, Al, Mg, Fe, S, OH, etc.), and in spectral scans (115 - 600 nm) to search for new species.

The VIRS and UVVS will measure surface reflectance at middle ultraviolet to visible to near infrared wavelengths to search for ferrous bearing minerals (spectral signatures near 1 μ), Fe-Ti bearing glasses (spectral signatures near 0.34 μ) and ferrous iron (strong band near 0.25 μ). These measurements will be made with a spatial resolution of 5 km or better.

4.1 ULTRAVIOLET-VISIBLE SPECTROMETER

The UVVS consists of a Cassegrain telescope and an Ebert-Fastie diffraction grating spectrometer. Its design is identical to the Galileo UVS except for two modifications. These are the installation of a new grating to extend the wavelength coverage and the addition of a two position mask at the spectrometer entrance slit to accommodate both atmospheric and surface reflectance observations.

The MASCS telescope has an effective focal length of 257 mm and a focal ratio of f/5. Its field of view can be changed from 1.0˚ x 0.04˚ for the atmospheric measurements to 0.05˚ x 0.04˚ for reflectance measurements by a two position mechanism which moves a mask with a 0.175 mm slot over the nominal 4.3 mm tall x 0.175 mm wide slit.

Table 4.1 MASCS Instrument Summary	
Telescope	
Focal length	257.6 mm
Aperture	50.3 x 52.8 mm
Ultraviolet and Visible Spectrometer	
Focal length	125 mm
Grating	2400 l/mm blazed at 330 nm
Spectral bandpass	0.3 nm FUV channel
	0.6 nm MUV, VIS channels
Wavelength range	
FUV channel	115-190 nm (2^{nd} order)
MUV channel	160-320 nm (1st order)
VIS-PMT channel	250-600 nm (1st order)
Field of view	
FUV, MUV, VIS	1° x 0.04° Atmosphere
FUV, MUV	0.05° x 0.04° Surface
Visible and Infrared Spectrometer	
Focal length	210 mm
Grating	100 l/mm
Spectral bandpass	5 nm
Wavelength range	
VIS channel	300 - 1050 nm
NIR channel	850 - 1450 nm
Field of view	0.023° circular
Instrument	
Mass	3.1 kg
Average power	6.1 Watts
Peak power	6.9 Watts
Envelop	195 x 205 x 310 mm
Nominal data rate	
VIRS	
UVVS	

This approach ensures that the UVVS can meet its primary measurements objectives even in the event of a mechanism failure. The telescope is equipped with an external light shade and an extensive baffle system for rejection of off-axis scattered light. Laboratory tests have demonstrated that the off axis rejection for this design is greater than 10^5 for point sources which are $\geq 1^{\circ}$ from the field of view (Hord et al. 1992).

The spectrometer is a standard, 125 mm focal length, Ebert-Fastie design. A ruling density of 2400 grooves per mm provides a first-order dispersion of 3 nm per mm and an average spectral resolution of 0.6 nm for a 0.175-mm-wide entrance slit (0.04˚ telescope field of view). Spectral scanning is accomplished by rotating the diffraction grating in discrete steps. Each step displaces the spectrum by 0.25 nm in the spectrometer focal plane resulting in an average spectral sampling frequency of 2.5 samples per resolution element.

Three Hamamatsu photomultiplier tubes, located behind separate exit slits in the spectrometer focal plane, are used in pulse counting mode for the atmospheric observations because very high sensitivity is required. These detectors are designated as Far Ultraviolet (FUV, 115 - 190 nm), Middle Ultraviolet (MUV, 160 - 320 nm), and Visible (VIS, 250 - 600 nm). Photocathodes and windows for these detectors are chosen to optimize measurements in narrow spectral ranges and minimize the effects of wavelength dependent scattered light within the spectrometer (Hord *et. al.* 1992). Both the FUV and MUV detectors may be used for surface reflectance measurements. We estimate that a 1 sec scan will provide a Signal-to-Noise ratio greater than 100 over the wavelength range $200 \leq \lambda \leq 300$ nm.

4.2 VISIBLE-INFRARED SPECTROGRAPH

The VIRS was added to the UVVS in order to measure surface reflectance in the wavelength range $0.3 \leq \lambda \leq 1.45$ μ. It is mounted to the top of the UVVS (See Figure 4.1). A 0.1 mm circular aperture located beside the UVVS entrance slit in the telescope focal plane defines the VIRS field of view to be 0.023˚ diameter. It is offset from the UVVS field of view by 0.38˚. Light from the telescope is fed to the VIRS through a fused silica fiber optics bundle located behind the aperture. The VIRS optical design consists of a flat field holographic concave diffraction grating which images the visible and near infrared spectrum onto two semiconductor detectors located in the spectrograph focal plane. A focal length of 210 mm and a ruling density of 100 grooves per mm result in a first-order dispersion of 50 nm per mm. A dichroic beam splitter located near the spectrograph focal plane separates visible (300 nm - 1050 nm) and infrared (0.90 - 1.45 μ) wavelengths before they are imaged onto the two detectors.

The visible spectrum is focused onto a Hamamatsu S3901-512Q Si diode array detector with 512 pixels that are 0.05 mm wide by 2.5 mm tall. This grating - detector combination provides a dispersion of 2.5 nm per pixel, requiring 340 pixels to cover the wavelength range 200 - 1050 nm with a resolution of 5 nm. Overlapping second order radiation from the grating is eliminated by placing a high-pass sharp cut-off absorption filter directly in front of the long wavelength half of the detector (Maymon *et. al.* 1988). Integration time and readout control logic for the detector are implemented using field programmable gate array technology. Charge read out from each pixel is integrated in a low-noise electrometer before being digitized with 16-bit precision. Based on our experience with Reticon detectors both for rocket-borne instruments and for the Russian Mars 94 mission, we expect the readout noise to be less than 5000 electrons. We chose the S3091 for its low dark current and anti-blooming circuitry. Our instrument sensitivity calculations indicate that a one second integration will result in a Signal-to-Noise ratio greater than 200 over the spectral range $0.3 \leq \lambda \leq 1.05$ μ when the detector operates at 20˚ C. At this temperature and integration time, dark current for a TB series contributes a negligible amount to detector saturation and noise.

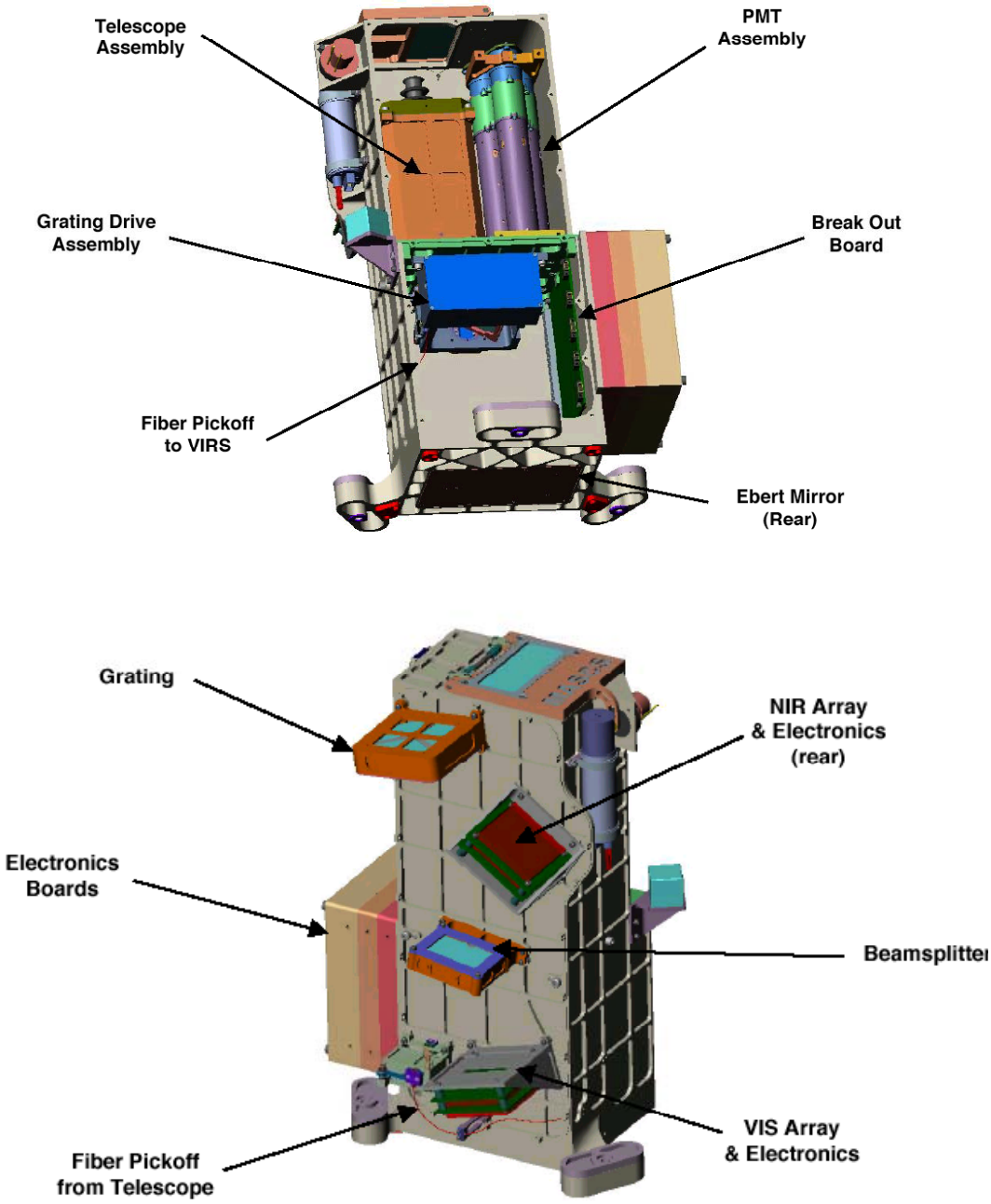

Figure 4.1 Mercury Atmospheric and Surface Composition Spectrometer. The top panel shows the telescope and UVVS internal components. The bottom panel shows the VIRS internal components.

Figure 4.1-A MASCS image

Wavelengths in the range 0.90 - 1.45 μ are focused onto a Hamahatsu G8162-256S Indium-Gallium-Arsenide (InGaAs) array with Multiplexed readout. This detector has an array of 256 InGaAs photodiodes, which are 0.05 mm wide by 0.5 mm tall. Integration time and readout control logic for the InGaAs array are also implemented using field programmable gate array technology. Voltages read out from the multiplex register can be directly digitized with 16-bit precision. The 9500 electrons read out noise in this device arises primarily from reset noise for individual amplifiers in the diode array. We chose InGaAs instead of germanium for the infrared detector because InGaAs does not require cooling. Our instrument sensitivity calculations indicate that we will achieve a SNR greater than 100 by summing for a two-second integration period. We chose 1.45 μ as the long wavelength cutoff for the VIRS because thermal emission from Mercury's surface is comparable to the solar reflectance beyond that wavelength.

5.0 CALIBRATION FACILITIES

MASCS unit-level and instrument-level calibrations were performed at LASP using in-house facilities. These facilities include the Calibration Test Equipment II (CTE II), Multi Optical Beam Instrumentation (MOBI), and a precision alignment facility consisting of a fixed collimator and a precision two-axis instrument rotation fixture (3.5 arc second angular resolution), both mounted on a vibration isolated optical bench.

UVVS detector quantum efficiency, spatial uniformity, and temporal stability were measured using the CTE II, which is a vacuum facility that provides a monochromatic, focused pencil beam that can be positioned using an externally manipulated steering mirror. Optical alignments including telescope boresight, spectrometer fields of view, telescope point spread function, telescope off axis response, and spectrometer polarization were all performed using the precision alignment fixture equipped with a variety of light sources as described in Section 6.

Spectrometer wavelength scales were determined using light sources to illuminate a white reflectance screen and in MOBI during thermal vacuum testing. MOBI is a large vacuum facility containing a four-axis instrument manipulator (two degrees of rotation and two degrees of translation) equipped with an instrument thermal control block and shroud. A telescope, attached to one end of the main vacuum tank and equipped with a monochromator at its focus, provides a collimated input beam to instruments under test. UVVS radiometric calibrations for wavelengths less than 250 nm were performed in MOBI before and after the formal instrument thermal vacuum testing. These calibrations use a photomultiplier detector, masked to a 2 mm^2 aperture and calibrated against a NIST photodiode, as a secondary standard to measure the average monochromatic photon flux (photons per second per unit area) arriving at the MASCS telescope aperture from the collimator. Instrument sensitivity (counts per irradiance unit) is simply the ratio of output counts to input beam flux as determined by the standard photomultiplier. The photomultiplier is rastered to map nonuniformities in the input beam, which are typically smaller than 10%.

Instrument-level radiometric calibrations for wavelengths greater than 250 nm for UVVS and for the entire VIRS wavelength range were preformed using irradiance standards (calibrated lamps) and a white reflectance screen. Screen properties (absolute reflectance and relative angular response) were characterized as described in Section 6.

The relative temperature dependence for spectrometer wavelength scale and point spread function, instrument radiometric sensitivity, and detector dark level and flat field were measured in MOBI during thermal vacuum testing.

6.0 INSTRUMENT-LEVEL CALIBRATIONS

Instrument functional testing preceded calibration. These tests verify proper function of operational modes, search for detector cross talk, and electrical interference from mechanisms (e.g. detector offsets, noise, or flat field response changes caused by mechanism actuation). In some cases correct function could only be completely verified during system-level calibration when the instrument is stimulated by a known source. Examples include data compression algorithms and detector cross talk. The instrument was also checked for light leaks during functional testing by illuminating it with a sun gun. Leaks resulting in detector output greater than 10% of the dark current (count rate for UVVS) were sealed before the formal instrument characterization/calibration. A particularly sensitive area for light leaks is located at the fitting where the nitrogen purge line enters the instrument at the rear of the UVVS spectrometer. Care must be taken to insure that the covering for the spacecraft purge line is sufficiently opaque to avoid compromising the visible photomultiplier detector within the UVVS.

The system level calibrations for the MASCS include telescope boresight alignment, spectrometer field of view, telescope point spread function and scattered light, wavelength scale, spectrometer point spread function and scattered light, radiometric sensitivity, and detector characteristics.

6.1 TELESCOPIC BORESIGHT

Figure 6.1 shows the locations on the plane of the sky for the nominal fields of view of the MASCS instrument as it looks out along the spacecraft +Z axis. The UVVS atmosphere slit, which is 1˚ tall by 0.04˚ wide, is oriented with its long axis parallel to the spacecraft Y axis. A movable mask with a 0.05˚ tall aperture, centered at the approximate midpoint of the atmosphere slit, defines the UVVS surface slit. The VIRS views the sky through a 0.023˚ circular aperture that is displaced by approximately 0.38˚ in the direction of the spacecraft -X axis.

During instrument calibration, telescope boresights (the centers of the fields of view) were measured relative to an instrument alignment cube for all three of these configurations. These data provide a convenient point of reference for the nominal fields of view during spacecraft integration and test. Since relative position of the telescope boresight with respect to the alignment cube and with respect to the instrument mounting feet depend on both MASCS case distortion and the motion of the telescope mirrors in their mechanical mountings, an accurate MASCS boresight relative to MDIS will be established after launch over the MASCS operational temperature range by using both star observations and observations of Mercury's limbs made at apoapsis. On the other hand, the relative position of the UVVS and VIRS boresights, which depends on the physical separation (approximately 2 mm) of their respective entrance apertures, is essentially independent of temperature and telescope mirror motion because both are mounted in a single monolithic aluminum bulkhead. (The MASCS thermal model indicates that gradients within the bulkhead are negligible for all MESSENGER operational temperatures.)

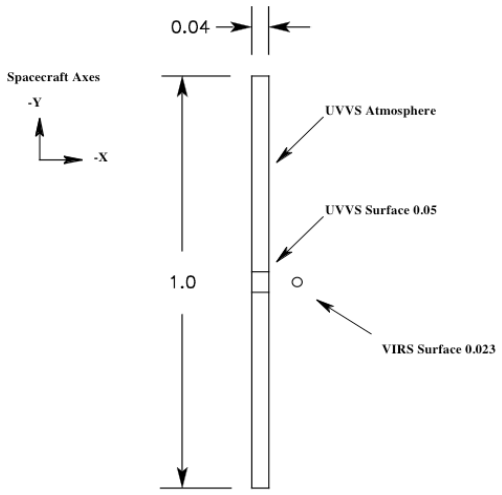

6.1.1 UVS Boresight Relative to the Instrument Reference Cube

The UVVS telescope boresight was measured relative to an alignment cube, which was mounted on instrument case, using a high precision (0.001˚ resolution) 2-axis gimbal and a 45-cm diameter, 229-cm focal length parabolic collimator mirror. A 0.25-mm diameter pinhole aperture, located at the mirror's focal point produce a reference beam that simulates a 'star source' with a 0.006˚ divergence.

First, a reference position for the front face of alignment cube was established by rotating the gimbal to autocollimate the reference beam. After the reference position was determined, the gimbal was rotated in order to place the image of the star source in the center of the UVVS field of view (See Section 6.2.1 for details.) and the angle was recorded.

The cube holder was equipped with steel alignment pins, which allowed it to be removed for instrument vibration testing. Removing and replacing the cube holder without disturbing the instrument or gimbal introduced shift as large as ±0.01˚ in the cube reference position. This uncertainty sets the accuracy limit for determining the relative alignment of the cube and telescope.

The boresight measurements were performed before and after instrument vibration in order to test the mechanical reproducibility of the telescope optics. Results are summarized in Table 6.1 and Figure 6.2 using a coordinate system in which the cube faces are aligned with the spacecraft axes. The values represent the angle through which the UVVS must be rotated in order to place the borsight on the reference cube axes, using a right-handed coordinate system.

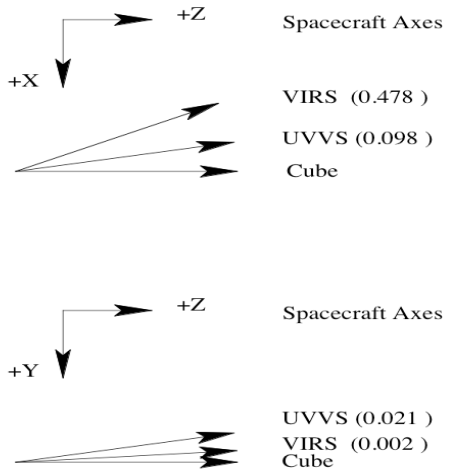

6.1.2 VIRS Boresight Relative to UVVS

Measurements of the VIRS entrance aperture relative the UVVS surface slit are described in 6.2.2 below and the results are included in Table 6.1.

Table 6.1 UVVS and VIRS Rotation Angles Relative to Reference Cube					
Slit	Aperature	Angle (Pre-Vibration)		Angle (Post-Vibration)	
		XZ Plane	YZ Plane	XZ Plane	YZ Plane
UVVS Atmosphere	1.0˚ x 0.04˚	+0.076˚	+0.026˚	+0.098˚	-0.021˚
UVVS Surface	0.05˚ x 0.04˚	+0.076˚	+0.016˚	+0.098˚	-0.031˚
VIRS	0.023˚ Dia			+0.478	-0.002

The rotation angles in Table 6.1 were converted into direction cosines for the three boresights and are recorded in Table 6.2.

Table 6.2 UVVS and VIRS Boresight Direction Cosines Relative to Reference Cube			
	X	Y	Z
UVVS Atmosphere	-0.00171	-0.00037	+0.999998
UVVS Surface	-0.00171	-0.00054	+0.999998
VIRS	-0.0083	-0.00003	+0.999965

No temperature characterization of boresight relative to the reference cube are required for MASCS since the ground alignment is expected to shift after launch and will also depend on the temperature induced distortions of the spacecraft mounting deck. This can affect the relative alignment of MASCS and MDIS and will be measured in flight by observing the calibration stars.

6.2 SPECTROMETER FIELDS OF VIEW

6.2.1 UVVS

Spectrometer field of view maps are primarily required for the UVVS because its photomultiplier tube detectors have relatively large spatial sensitivity variations. The VIS and MUV Fields of View (FOVs) were measured using the precision gimbal and collimator described in Section 6.1.1 to scan a star image first across the center of the UVVS entrance slit (dispersion direction) and then along its length. Both atmosphere and surface modes were observed. The FUV channel atmosphere-mode FOV was measured using the collimator and two-axis gimbal in the thermal vacuum/ vacuum radiometric calibration facility. The UVVS atmosphere mode FOV results are plotted in Figure 6.3 where the left panel shows the VIS detector dispersion scan. Scans for the MUV and FUV are virtually identical because the telescope PSF rather than the variations in detector sensitivity dominates the response.

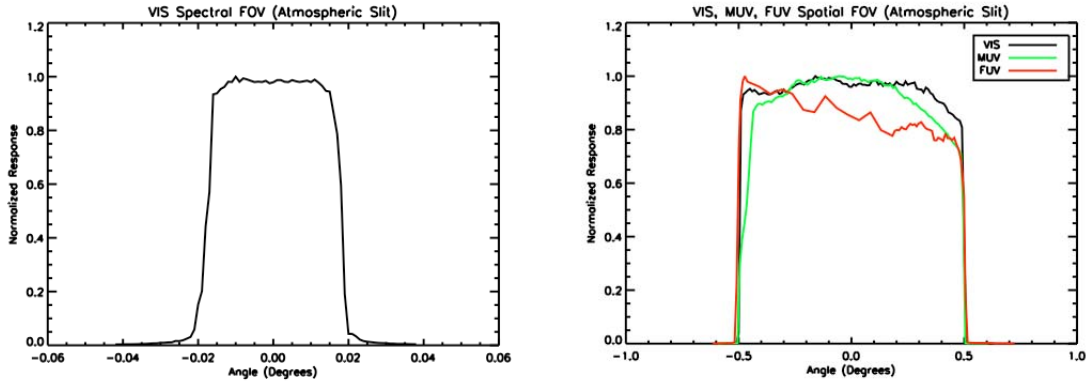

Scans along the slit (right panel) show small variations from detector to detector. Linear fits to the sharp image cutoffs (100% attenuation in 0.005 degrees) at the FOV edges suggest that the greater than 90% of the light from the telescope image is contained within a 0.01 mm diameter blur spot.

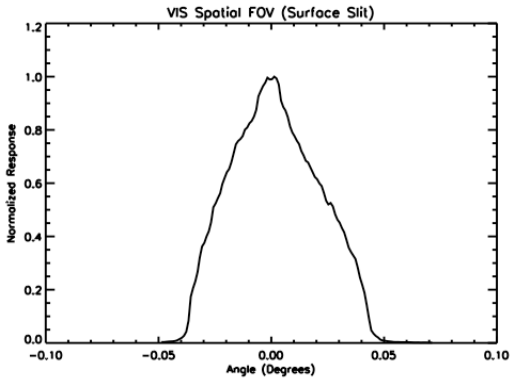

Figure 6.4 UVVS surface slit spatial FOV

Figure 6.4 shows the UVVS surface mode FOV for the VIS and MUV channels. When the spectrometer is placed in surface mode, the shutter knife edges, which are designed to provide a nominal 0.05˚ tall FOV, are displaced, by design, approximately 0.75 mm behind the telescope focal plane. This causes the light that enters the spectrometer at the top and of the surface slit to be out of focus smearing the cross-dispersion edges of the FOV.

6.2.2 VIRS Field of View

Maps of the VIRS FOV were used to determine the VIRS boresight and field of view and to infer the telescope point spread function (PSF). The VIRS FOV (nominal 0.023˚ circle) was measured by stepping the star source across the telescope image plane to obtain 121 spectra over an 0.08˚ square grid (11 x 11 images separated by 0.008˚). The zero position for the grid was set to the center of the UVVS surface slit.

Figure 6.5 shows a surface plot of the resulting field of view map where each data value is the sum of an entire VIRS VIS array detector spectrum after background subtraction. The position and width of the FOV in the horizontal and vertical directions was found by fitting a Gaussian to vertical and horizontal summed curves, respectively.

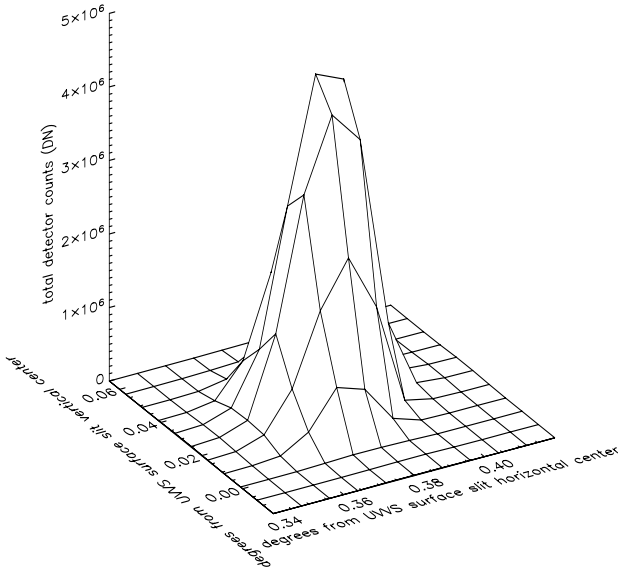

Figure 6.5 VIRS Field of View

The position was found to be 0.380º from the center of the UVVS surface slit in the dispersion direction, and 0.029º in the cross dispersion direction. The 0.022˚ full width half maxima of the two Gaussian fits are in good agreement with the 0.023º nominal FOV.

6.2.3 Telescope PSF

A contour plot of the VIRS FOV, which is shown in Figure 6.6, displays a small amount of coma. This result is consistent with the telescope ray trace model for the imaging performance of a Dall-Kirkham two-mirror telescope with a 0.023˚ circular FOV located 0.38˚ off axis.

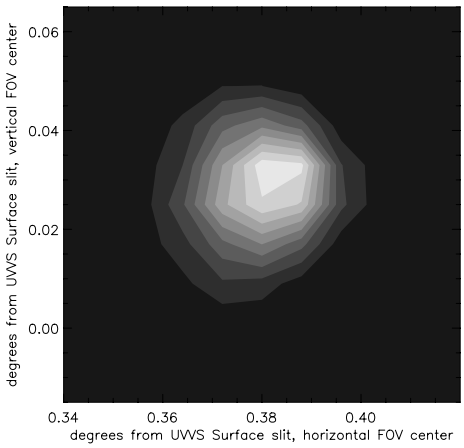

Figure 6.6 Contour plot of the VIS FOV

These measurements were performed in the laboratory at a temperature of 20˚ C. The telescope mirrors are made from ultra low expansion optical glass and metered by invar spacer rods. Ray trace analysis indicated that for this design approach the FWHM of the telescope point spread function varies by less than 10% over the MASCS operational temperature range (-30˚ C to +30˚ C).

Any temperature-induced shifts in the telescope boresight relative to spacecraft mounting resulting form distortions in the MASCS instrument case that could affect the MASCS to MDIS alignment will be characterized after launch by observing stars during cruise and the planet limb once the spacecraft is in orbit around Mercury.

6.3 TELESCOPIC OFF-AXIS RESPONSE

MASCS uses limb scan observations to observe faint atmospheric emissions above the limb of the sunlit disk of Mercury. Good off-axis rejection allows the UVVS to operate at greater distances from the planet, maximizing atmospheric observation time.

The telescope off-axis response was measured using the precision gimbal and collimator described in Section 6.1.1 to scan a star image first across the center of the UVVS entrance slit (dispersion direction) and then along its length. Scans were made over ±5˚ swaths away from the nominal 0.1˚ x 1.0˚ FOV in order to assess what fraction of light entering the telescope 'off axis' was recorded by the spectrometer as signal.

The collimator was equipped with a mercury 'penray' lamp, which produces a bright emission line at 253.7 nm, and the measurements were made with the MUV detector used in mini-scan mode (short

scans over a narrow wavelength interval centered on 253.7 nm) in order to minimize contamination from background sources in the room.

In order to increase the dynamic range of the measurement a neutral density filter was inserted between the lamp and the collimator pinhole when the image of the star source fell within the UVVS entrance slit. The filter was removed for gimbal angles that placed the image of the star source outside the entrance slit. This increased the light intensity entering the telescope by ~ a factor of 100. A precise value for the filter transmission was measured by allowing for overlap in scan ranges between the 'filter in' and 'filter out' measurements. The manipulator was stepped at a high angular resolution as the star source moved across the entrance slit, and then in the interest of time the angular step resolution was decreased for the other data sets.

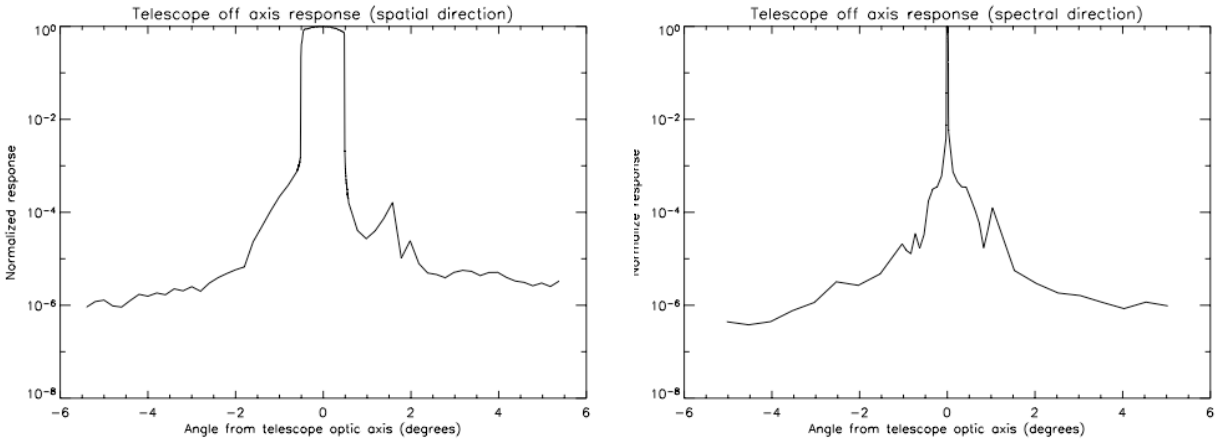

Figure 6.7 MASCS Telescope off-axis response in the dispersion direction (left panel) and the cross dispersion direction (right panel)

The measured off-axis response is shown in Figure 6.7 for the spectrometer dispersion (right panel) and cross-dispersion (left panel) directions. These data indicate that the signal for a point source decreases by about 4 orders of magnitude when the image is greater than 0.5˚ from the edge of the spectrometer field of view, declining to ~ 6 orders of magnitude at 5˚.

The noticeable ~ factor of 10 increase in the dispersion direction response, which occurs at 1.1˚, is caused by an asymmetry in the primary mirror central baffle required to accommodate the VIRS spectrometer entrance aperture 0.38˚ off axis. The cause for a similar increase seen at 1.75˚ in the cross-dispersion direction has not been identified. Values shown in Figure 6.7 for angles greater than 4˚ may overestimate the true off axis response because it is difficult to prevent light scattered from the penray lamp by laboratory surroundings from entering the telescope aperture.

6.4 SPECTROMETER WAVELENGTH SCALE

Wavelength calibration and spectrometer point spread function use a deuterium lamp for $\lambda<185$ nm and emission line sources (pen-ray and microwave discharge lamps) for $\lambda>185$ nm. Accurate determination

requires that the instrument full aperture and field of view be filled. This was accomplished by observing a white reflectance screen and a collimator with diffuser screen, rather than a pinhole, placed at the focus. Wavelength measurements over the operational temperature range characterize spectrometer mechanical distortions.

6.4.1 UVVS

The UVVS wavelength scale is determined by the equation for an Ebert-Fastie spectrometer

$$m\lambda = 2d\sin(\theta)\cos(\phi) \qquad 6.1$$
$$\theta = \frac{(\beta + \alpha)}{2}$$
$$\phi = \frac{(\beta - \alpha)}{2}$$

where λ is the wavelength, d is the grating spacing, m is the diffraction order number, α is the angle of incidence and β is the angle of diffraction. ϕ is the half angle difference, which is fixed by the geometry of the spectrometer for each channel. $\theta = \alpha + \phi$ is the grating rotation angle. $\alpha = (A + n*\Delta)$ where A is a constant determined by the grating mount, Δ is the grating step size, and n an integer between 0 and 2400. For UVVS the nominal grating step size at room temperature (~20˚ C) is $\Delta = 0.0167$˚ (1 arc minute) and the grating spacing is d = 416.667 nm (2400 grooves mm^{-1}).

Values for A and Δ and for ϕ for the VIS channel were determined at room temperature (20˚ C) by least-squares fitting equation 6.1 to spectra from a mercury penray lamp and a mercury microwave discharge lamp illuminating a white reflectance screen. Typically four to six isolated wavelengths were used to calculate A, Δ, and ϕ. For the FUV and MUV channel, a single measurement of 253.7 nm was used to determine ϕ assuming values of A and Δ obtained for VIS. Line centers, n_J, were determined by fitting Gaussian profiles to the observed lines. Wavelengths, λ_J, were air values obtained from NIST standard tables. The values for ϕ, Δ, and A were found to be $\phi = 9.998$, 12.332, and 14.673 degrees for the VIS, MUV, and FUV channels respectively, $\Delta = 0.016665$ degrees, and A = -2.020 degrees. Inserting these values into the equation for an Ebert-Fastie spectrometer and recalling that the VIS and MUV are first order while the FUV is second order gives:

$$\lambda = 403.079 \bullet \sin(12.652 + 0.016665 \bullet n) \text{ nm (FUV)}$$
$$\lambda = 814.105 \bullet \sin(10.312 + 0.016665 \bullet n) \text{ nm (MUV)} \qquad 6.2$$
$$\lambda = 820.679 \bullet \sin(7.977 + 0.016665 \bullet n) \text{ nm (VIS)}$$

A plot of wavelength versus grating step position is given in figure 6.8 for each channel. Residual errors in the derived wavelength scale are shown in Figure 6.9. These values are less that 1% of the instrument bandpass, which is greater than 2.9 grating steps wide across the entire wavelength range (see discussion below).

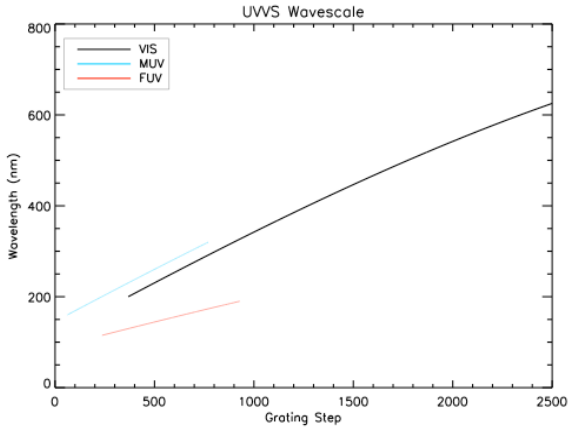

Figure 6.8 UVVS wavelength versus grating drive step position.

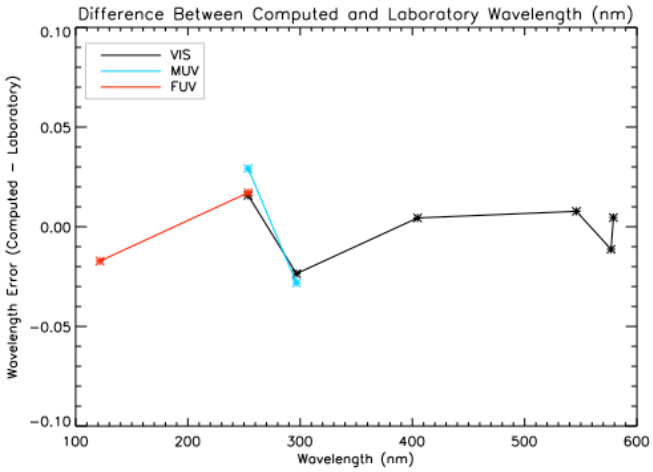

Figure 6.9 Residual errors in the UVVS wavelength scale

Shifts in wavelength scale were measured over a temperature range of $-27^{\circ}C$ to $+36^{\circ}C$ by monitoring the position of a single emission line over one temperature cycle during thermal vacuum testing. A collimator with a diffuser at its focus was used to simultaneously fill both the UVVS and VIRS FOVs. Line positions were determined by fitting Gaussians to sixteen step wide 'mini scans' obtained for each channel at each dwell temperature in the thermal vacuum cycle. Figure 6.10 shows the deviation of line center from the average step position. All three channels display nearly identical temperature dependence even though the selected lines appear over a wide range of grating position (~ step 450 for MUV and FUV and ~ step 2200 for VIS), suggesting that the observed displacement is caused by instrument case distortion rather than changes in grating drive step size. The total deviation is approximately 0.3 grating steps, which is equivalent to a displacement of 0.02 mm in the spectrometer focal plane.

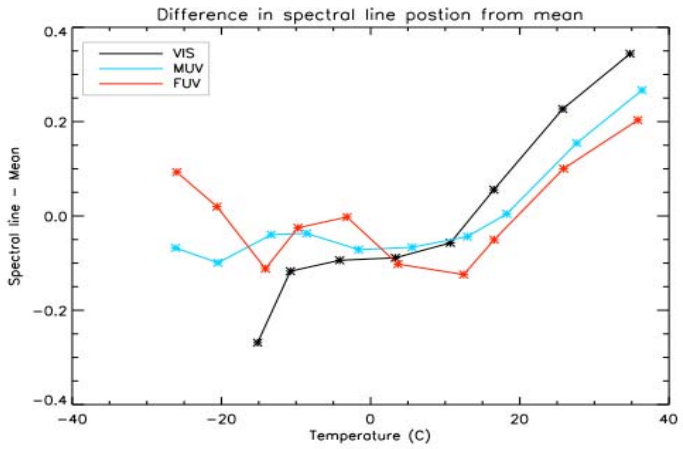

Figure 6.10 UVVS wavelength scale shift as a function of temperature

6.4.2 VIRS

The VIRS spectrometer uses a flat field holographic grating to image the spectrum flat focal plane. Its wavelength scale is determined from the standard grating equation with the output projected onto a straight line whose normal is rotated through an angle β_0 with respect to the grating normal:

$$\sin(\beta) = \frac{\lambda}{d} - \sin(\alpha) \qquad 6.3$$

$$x_\lambda = l \bullet \tan(\beta - \beta_0)$$

where α = -9.02˚, d=10^4 nm, and l~206.0 mm. Detector pixel number, n_λ, is related to focal plane displacement, x_λ, is related: $n_\lambda = x_\lambda / 0.050$. The wavelength scale defined equations 6.4 can be approximated by a quadratic relating or pixel number to wavelength:

$$\lambda = \lambda_0 + A \bullet n_\lambda + B \bullet n_\lambda^2 \qquad 6.4$$

The constants A, B, and λ_0 were determined separately for NIR and VIS at room temperature (20˚ C) by least-squares fitting equation 6.4 to spectra from a mercury microwave discharge lamp. Line centers, n_J, were determined both by fitting Gaussian profiles to and by calculation the centroids of the observed lines. Wavelengths for which the Gaussian and centroid centers differed by more than 0.15 pixels were deleted from the fit, providing four and five unambiguous wavelengths for NIR and VIS respectively. Wavelengths, λ_J, were air values obtained from NIST standard tables. Inserting the values for λ_0, A, and B for each detector into equation 6.4 gives:

A plot of wavelength versus pixel location is given in figure 6.11 for both NIR and VIS detectors. Figure 6.12 shows a plot of the residual errors in the wavelength scale for these parameters. The Maximum deviation from the fit is 0.07 nm for the VIS, 0.02 nm for the NIR, which is less than 2% of the nominal instrument bandpass.

$$\lambda = 215.16 + 2.330 \bullet n - 1.89x10^{-5} \bullet n^2 \text{ nm (VIS)} \qquad 6.5$$

$$\lambda = 896.50 + 2.330 \bullet n + 1.48x10^{-5} \bullet n^2 \text{ nm (NIR)}$$

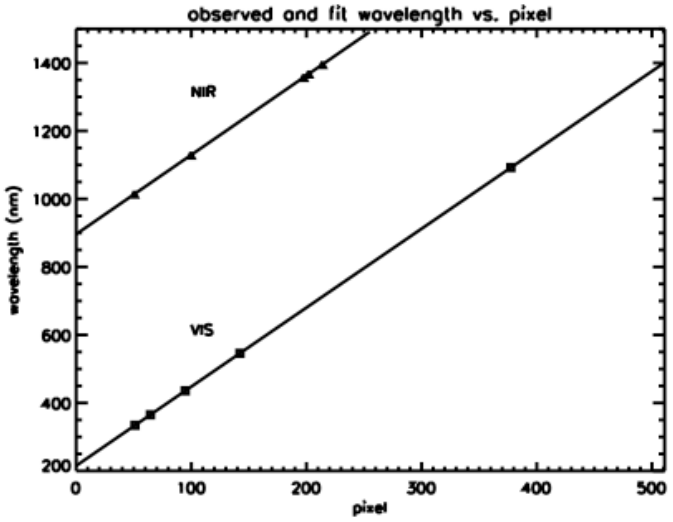

Figure 6.11 VIS and NIR wavelength scales

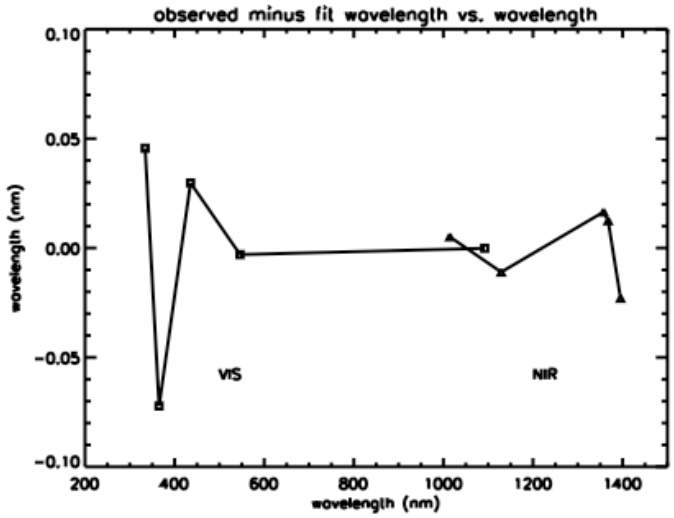

Figure 6.12 Residual errors in the VIRS wavelength scale

Shifts in wavelength scale were measured over a temperature range of $-27^{\circ}\mathrm{C}$ to $+36^{\circ}\mathrm{C}$ during thermal vacuum testing using a collimator with a diffuser at its focus to fill the VIRS FOV. The constants in equation 6.5 were determined for each temperature to derive an average wavelength shift over each detector. Input lamp intensity drift during the temperature cycle precluded NIR measurements for temperatures greater than 0˚ C. Results are plotted in Figure 6.13 for the observed shifts. The total excursion in the wavelength scale is 1.25 nm, which is equivalent to a 0.027 mm shift of the spectrum on the detectors. This is similar in magnitude to the shifts observed for the UVVS wavelength scale.

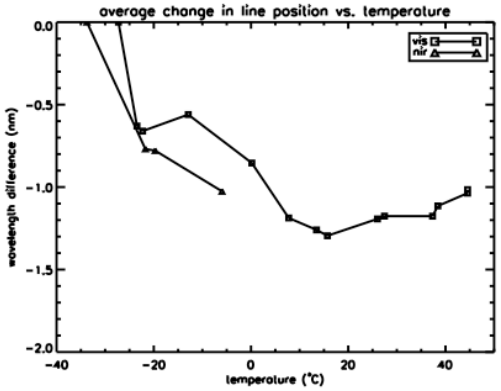

Figure 6.13 VIRS wavelength shift as a function of temperature

6.5 SPECTROMETER POINT SPREAD FUNCTION

Because UVVS is a scanning grating monochromator with detectors behind fixed exit slits, its point spread function (PSF) is dominated by the spectrometer imaging performance. On the other hand, the VIRS grating images its output spectrum onto array detectors, each of which has a characteristic PSF and it is the convolution of optics and grating that produces the system PSF.

6.5.1 UVVS

The UVVS imaging function for a monochromatic line is the convolution of the image of the entrance slit with the physical width of the exit slit. In the absence of image aberration, the entrance slit image width is given by:

$$w'_{en} = w_{en} \cdot \cos(\alpha) / \cos(\beta)$$

The ratio of cosines is referred to as anamorphic magnification. For an Ebert-Fastie configuration, the image of the entrance slit is always larger than the slit itself. The resulting imaging function is a trapezoid with a Full Width Half Maximum (FWHM) equal to the greater of the entrance slit image or the exit slit width. Differentiating the standard grating equation with respect to the diffraction angle, β, and multiplying by the angular width of the imaging function gives an expression for the spectrometer band pass. $\Delta\lambda$,

$$\Delta\lambda = \frac{d}{m \cdot F_l} \cdot \cos(\beta) \cdot w_{ex} \quad when \ \cos(\beta) \cdot w_{ex} > \cos(\alpha) \cdot w_{en}$$
$$\Delta\lambda = \frac{d}{m \cdot F_l} \cdot \cos(\alpha) \cdot w_{en} \quad when \ \cos(\alpha) \cdot w_{en} > \cos(\beta) \cdot w_{ex} \qquad 6.6$$

where d = 416.667 nm is the grating spacing, F_l-=125 mm is the spectrometer focal length, and w_{en} and w_{ex} have values of 0.175 mm and 0.23 mm respectively. Bandpass and grating step size are plotted in Figure 6.14 for the three UVVS channels using the diffraction angle values derived from the wavelength scale fitting.

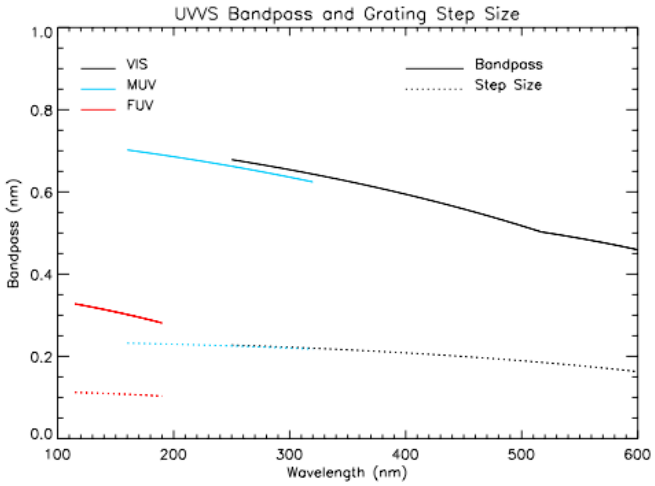

Figure 6.14 UVVS bandpass and grating step size

The UVVS PSF is a convolution of a trapezoidal bandpass, described by Equations 6.6 above, and the optical PSF. In practice the resulting system PSF can be approximated by a Gaussian function, which is illustrated in Figure 6.15 where the symbols are the discrete data samples for an VIS channel scan of the 253.7 nm line from a Mercury penray lamp illuminating a reflectance screen to fill both the aperture and field of view of the UVVS. The solid line is a Gaussian fit to the data, which has a FWHM of 2.7 grating steps. This value is slightly smaller than the 2.9 steps FWHM computed from the bandpass shown in Figure 6.14 (bandpass = 0.68 nm and step size = 0.23 nm). Fits to the 253.7 nm line for the MUV and FUV channels produce similar results.

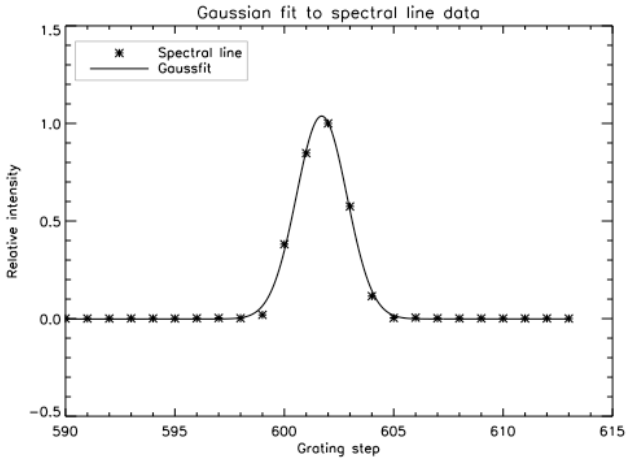

Figure 6.15 The UVVS Point Spread Function is well approximated by a Gaussian with FWHM = 2.7 steps

Both the bandpass function and optical PSF are a weak function of wavelength and temperature. These dependences are illustrated in Figure 6.16 where the left panel is a plot of FWHM versus grating step number for the three channels and versus temperature in the right panel. The grating step dependence is consistent with bandpass and grating step size calculations shown in Figure 6.14, which suggest that FWHM, measured in grating steps, should increase slightly with increasing wavelength. Fits to the wavelength scale data acquired during thermal vacuum testing indicate that the UVVS PSF width increases by approximately 5% as the instrument cools from room temperature to –25˚ C. This is most likely the result of a change in focal distance caused by a decrease in spectrometer case dimension.

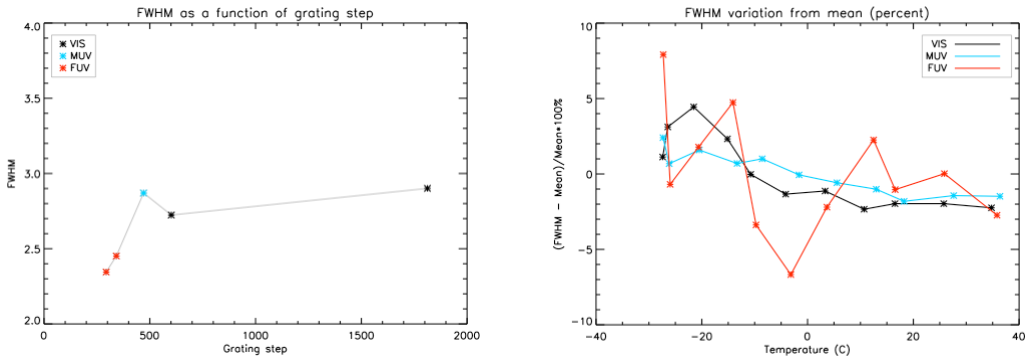

Figure 6.16 UVVS Point Spread Function is weakly dependent on grating step position (left panel) and temperature (right panel)

Most emissions from the Mercury exosphere are expected to be isolated and optically thin. An important exception is the sodium D lines at λλ 588.995 and 589.592 nm. A key requirement for MASCS is to resolve these lines with sufficient accuracy that the relative intensities of the two components can be determined. This was verified during calibration using a sodium lamp to illuminate a reflectance screen. The spectrum recorded by the UVVS, which is shown in Figure 6.17, has the D lines cleanly resolved demonstrating that the UVVS meets this measurement requirement.

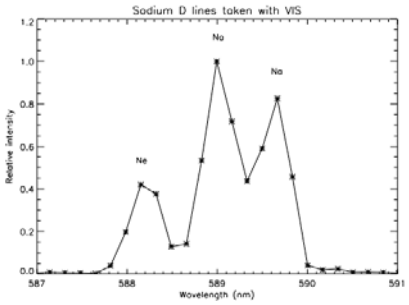

Figure 6.17 The UVVS cleanly resolves the sodium D lines near 589.3 nm

FSCM NO.	SIZE	DRAWING NO.	REV.
88898	A	7384-9470	A
SCALE	DO NOT SCALE PRINT	SHEET 29 of 49	

6.5.2 VIRS

Bandpass and dispersion relationships for VIRS are very nearly constant across the entire wavelength

$$\frac{d\lambda}{dx} = \frac{d}{F_l} = 46.6 nm/mm \qquad 6.7$$

$$\Delta\lambda = \frac{d}{F_l} \cdot w_{en} = 4.66 nm$$

range because the grating operates at near normal incidence. Thus the bandpass is determined by the image of the 0.1 mm diameter fiber input. VIRS final PSF is the convolution of the grating image and the PSF for the two VIRS detectors. VIS detector pixels are composed of 0.045 mm wide photo sites spaced 0.050 mm apart, resulting in a nearly rectangular pixel response. NIR detectors pixels are 0.030 mm wide spaced 0.050 mm apart so that response function is trapezoidal with a 0.05 mm FWHM and a 0.070 mm wide full width at the base. The grating image for a 0.10 mm diameter pinhole is astigmatic with a height that varies from 1.5 mm near 250 nm to 0.3 mm near 1000 nm. Its width is very nearly 0.1 mm wide across the entire field, with a low-energy coma flare toward the long wavelength side. Ray trace analysis shows that aberrations from the beam splitter and a condensing lens mounted on the front of the NIR detector smear the image arriving at the NIR detector by about 0.03 mm FWHM.

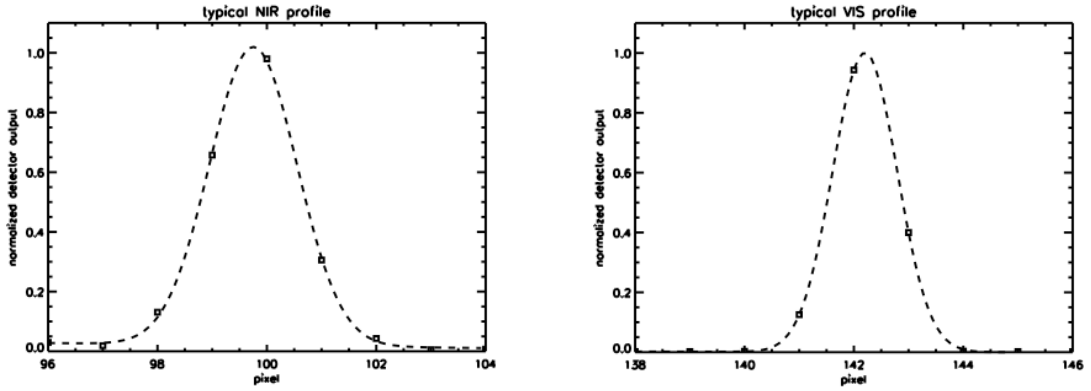

Figure 6.18 NIR (left panel) and VIS (right panel) point spread functions

Figure 6.18 shows representative plots of the VIRS PSF for both the VIS and NIR detector, obtained from spectra of a mercury discharge lamp. Dashed lines are Gaussian fits to the data, which have FWHM of 1.39 (3.23 nm) and 1.88 (4.38 nm) pixels for the VIS and NIR respectively. These values are consistent with the results from the simulations described above. Plots of the PSF FWHM as a function of temperature are shown in Figure 6.19. These data were acquired during thermal vacuum testing except for the single NIR value at 27˚ (shown as a triangle), which was acquired at ambient conditions. These results indicate that the VIRS spectral resolution is essentially independent of temperature over the range –10˚ to + 40˚ C.

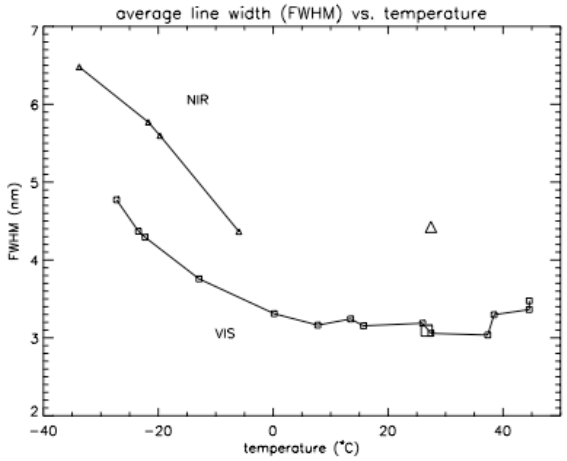

Figure 6.19 VIRS point spread function FWHM versus temperature

6.6 SPECTROMETER SCATTERED LIGHT

Scattered light measurements at the system level include the combination of optical element scatter plus diffuse and stray light present in the assembled spectrometer. Optical element scatter is usually dominated by diffraction grating performance, where scatter at wavelengths close to a parent emission is determined by the number of illuminated grating grooves and is wavelength independent. The far wings of the grating scatter function and diffuse scatter vary inversely with wavelength. Monochromatic scattered light characterizations are important for identifying glints and direct stray light paths in the assembled instrument. Usually these contributions are substantially larger than wings produced by a high quality diffraction grating.

MASCS scattered light measurements were performed using lasers to provide bright monochromatic sources for both the UVVS and VIRS. Only a single laser wavelength was available for the UVVS VIS channel. MUV scattering characteristics were inferred by comparing MUV and VIS scans of a single bright line from a mercury penray lamp. No scatter measurements were made for the UVVS FUV channel. Two laser wavelengths were used to measure VIRS scatter.

6.6.1 UVVS

Figure 6.20 is a VIS spectrum of a 532 nm laser used to characterize UVVS point spread function and scattered light. These data were assembled from three separate, overlapping scans. The first two measured the profile wings on either side of line center with an unattenuated laser. A 10^3 neutral density filter was then inserted in the laser beam for the final scan of the line core. With the exception of a distinctive lobe located 35 grating steps to the left of the peak emission, the composite scan is the classic profile for scatter in a high quality plane grating spectrometer with a residual level ~ 10^{-5} of the central peak per VIS bandpass (0.6 nm) in the far wings. The lobe has been identified as a glint from one wall of the grating housing support structure that affects only the VIS detector. Its integrated intensity was estimated to be 0.5 percent of the central peak by reflecting the inner wing of left side of the profile about line center (dashed line) to estimate the contribution from grating scatter

alone. There is evidence for a second lobe 100 steps to the right of the central peak, which has a relative intensity less than 10^{-4}. The total scatter outside the point spread function (± 3 grating positions from line center), integrated over the VIS wavelength range but excluding the glint lobe, is ~1.8% with 1.6% contained in the inner wings, which are ± 6 grating steps from line center. Neither scattering lobe presents an obstacle to UVVS data analysis but researchers should be aware that very low-level VIS emissions next to bright lines can be instrument scattered light artifacts.

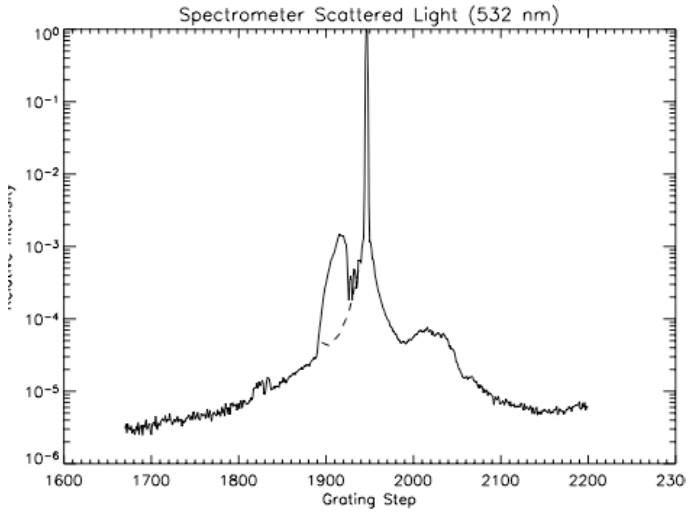

Figure 6.20 UVVS scattered light profile for VIS showing a glint for –35 grating steps

Figure 6.21 compares the VIS and MUV profiles for the 236.5 nm mercury line. Except for the absence of the glint lobe in the MUV data, the two profiles agree suggesting that the profile shown in Figure 6.20 with the glint lobe removed is a good approximation for the MUV profile.

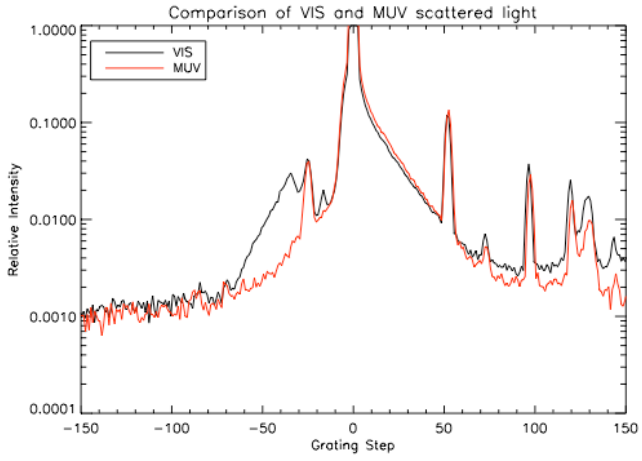

Figure 6.21 UVVS VIS and MUV scattered light comparison. No glint is apparent for MUV.

6.6.2 VIRS

VIRS scattered light was measured for the VIS and NIR detectors using a pair of lasers with wavelengths of 532 nm and 1064 nm respectively. Figure 6.22 shows the observed profiles for both VIS (left panel) and NIR (right panel), which have been normalized to unit area. Both profiles show an asymmetry in the far wings with the short wavelength side showing larger values. The integrated scatter in the wings (greater than ± 2 pixels for VIS and ± 3 pixels for NIR) is 2.3% and 4.1% respectively.

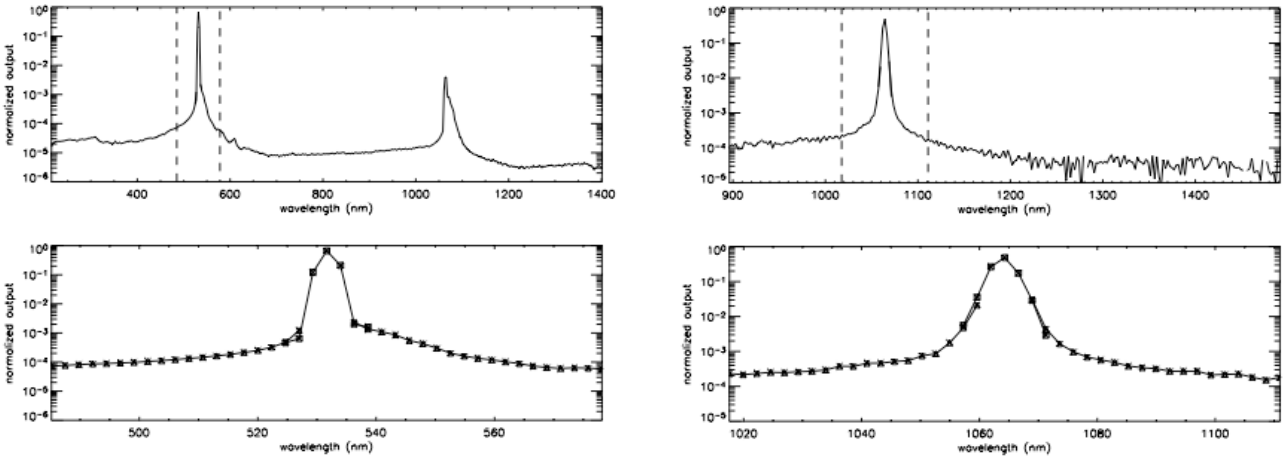

Figure 6.22 VIS (left panel) and NIR (right panel) scattered light profiles

Figure 6.23 is a VIS profile of the 1064 nm laser. The broad wings at 10^{-2} result from photon diffusion within the detector substrate rather than optical scatter within the spectrograph. Here the energy in the far scatter wings is an order of magnitude larger than for 532 nm.

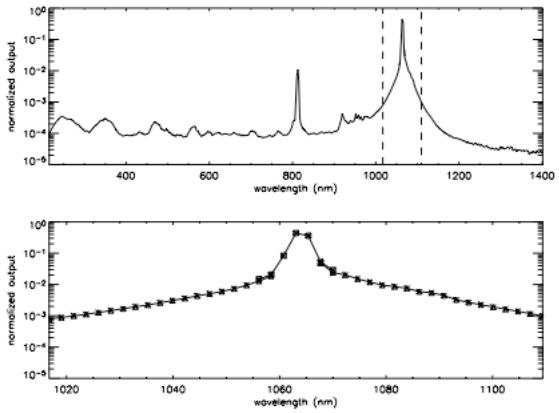

Figure 6.23 VIS profile for 1064 nm showing internal detector scatter

6.6.3 Grating Scatter Corrections

The MASCS spectrometer point spread functions, which are shown in Figures 6.20 – 6.23 are convolutions of an imaging point spread function and a grating scatter function, which can be approximated as a Lorentzian profile plus a constant; that is, PSF=IPSF⊗GSF. Because the grating scatter component in the point spread function for both spectrometers is relatively small, there is a simple algorithm for estimating its magnitude from the observed spectrum: Let *S* be the spectrum that would be observed in the absence of scatter, but including the IPSF. The observed spectrum, $O = S \otimes GSF$, can be represented as the sum of two components, $O = S + S_{Scat}$, where the scatter term is the difference between O and S, $S_{Scat} = S \otimes GSF - S$. If the convolution of the scatter term with the GSF can be ignored, then S_{Sca} can be approximated by $O \otimes GSF - O$. A simple model to illustrate this approach is shown in Figure 6.24. The left panel is a VIS detector model calculation for a reflected solar spectrum, *S*, which includes the VIRS sensitivity and IPSF, but no contribution from the GSF. The black line is the scattered light contribution that must be added to *S* to produce a complete model spectrum that includes grating scatter, $S_{Scat} = S \otimes GSF - S$ and the red curve is the estimate for $S_{Scat} \sim O \otimes GSF - O$. The agreement between these two curves indicates that the scatter term calculated directly from the model spectrum can be estimated to within better than 2% from the difference $O \otimes GSF - O$. This approach is much simpler than a deconvolution based on transforms and was used to estimate grating scattered light contribution to the instrument radiometric sensitivity for both UVVS and VIRS (Section 6.8).

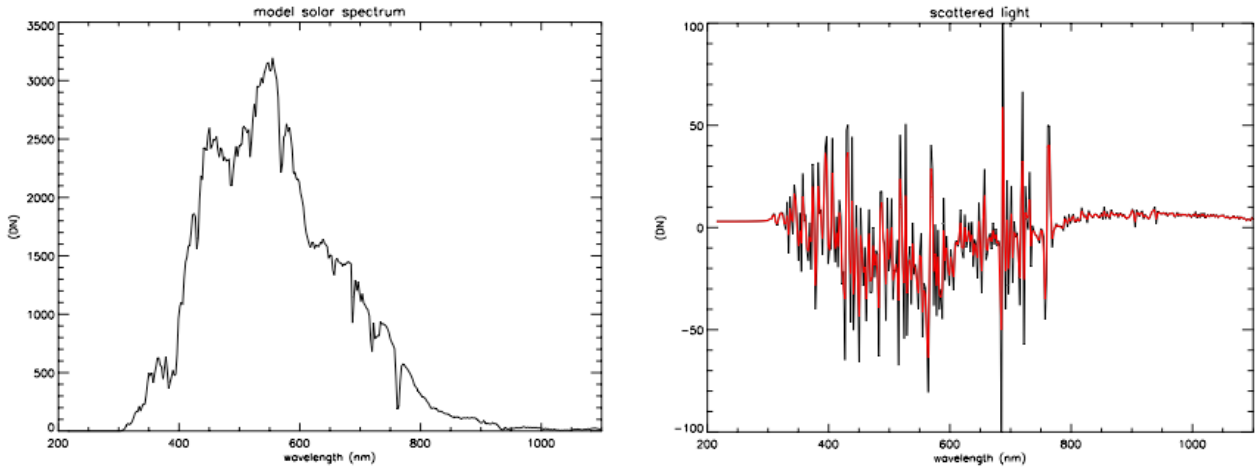

Figure 6.24 Grating scatter calculations. The left panel shows a model solar observation, excluding any grating scatter contribution. The black curve in the right panel is the calculated grating scatter and the red curve is an estimate.

6.7 SPECTROMETER POLARIZATION

It is unlikely that the instrument response to polarized light will be required to analyze MASCS data. Nonetheless polarization was measured for wavelengths greater than 210 nm as part of the overall instrument characterization. A polarized beam was produced using Glan-Taylor prism polarizer to feed a laboratory collimator. Parallel and perpendicular components were measured by rotating the MASCS instrument about the telescope boresight to place the grating grooves of the UVVS and VIRS first

parallel to and then perpendicular to the direction of the incident electric vector. Instrument polarization response is then plotted as the ratio $(I_{perp} - I_{para})/(I_{perp} + I_{para})$.

Figure 6.25 summarizes the UVVS polarization response where the black and red curves were calculated from data taken with a deuterium lamp as the input source to the collimator. A quartz halogen lamp was used to extend the VIS channel results from 500 nm to 620 nm (blue curve).

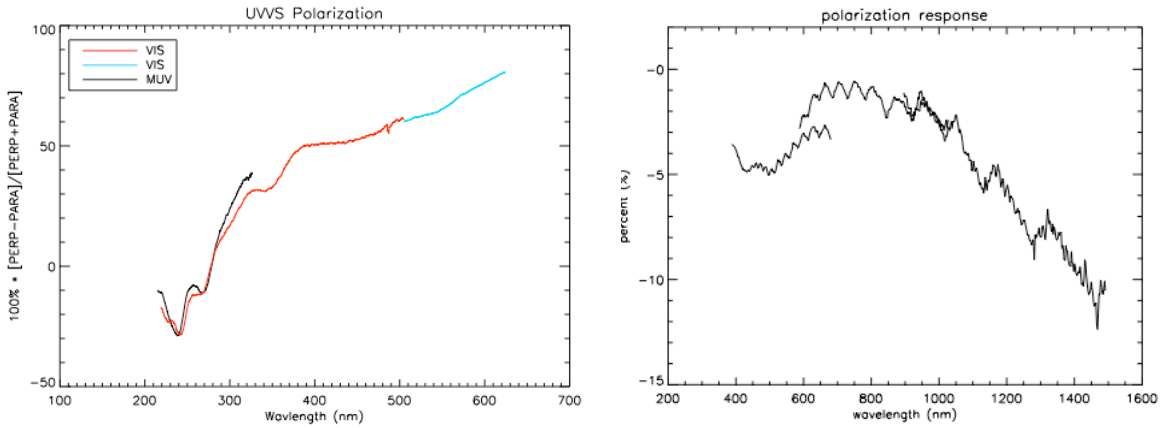

Figure 6.25 UVVS (left panel) and VIRS (right panel) polarization

6.8 RADIOMETRIC SENSITIVITY

MASCS radiometric calibrations were based on National Institute for Standards and Technology (NIST) source standards (calibrated lamps) and detector standards (calibrated photodiodes). Source standards were used to illuminate a screen coated with Kodak White Reflectance Coating (REF), which produces a source that fills telescope aperture and spectrometer field of view, for calibrating VIRS, UVVS VIS, and part of UVVS MUV at wavelengths greater than 200 nm. Screen radiance values were calculated by dividing screen reflectance, taken from vendor specifications (typically > 0.95 for $\lambda > 250$ nm), by π and then by lamp irradiance values from the lamp calibration data, which was typically reported at a wavelength cadence of 10 nm. Lamp irradiance at intermediate wavelength values was estimated by linearly interpolating values from the data sheet.

UVVS calibrations for wavelengths less than 320 nm (FUV and MUV) were performed in vacuum using a star source equipped with a monochromator to produce a collimated, monochromatic, irradiance source. The irradiance arriving at the MASCS telescope aperture was measured using a pulse-counting phtotmultiplier, which was calibrated for absolute sensitivity using a NIST-calibrated photodiode to scan the collimated input beam.

For both calibration configurations, instrument output was converted to radiance input from continuous spectral sources using the following relation:

$$L(\lambda_j) = \frac{[C(\lambda_j)\cdot N(C) - D(j) - S_l'(\lambda_j) - Stray(\lambda_j)]/\Delta t}{A\cdot\Delta\lambda\cdot R_c(\lambda_j)\cdot FF_j\cdot\overline{\Omega}\cdot(1-S_l)} = \frac{C_{Corr}(\lambda_j)/\Delta t}{A\cdot\Delta\lambda\cdot R_c(\lambda_j)\cdot\overline{\Omega}} \qquad 6.8$$

Here, L is radiance per unit wavelength interval (e.g. Watts per square cm per steradian per nanometer). *C* is either the photomultiplier counts at grating position J or VIRS array data number for pixel J obtained during integration time, Δt, *N* is the detector linearity correction, which includes analog-to-digital converter errors for the VIRS arrays, and *D* is the dark-count or dark-current data-number correction. *A* is the area of the telescope, $\Delta\lambda$ is the spectral bandpass, R_c is the instrument responsivity at the center of the FOV for a detector array with uniform pixel sensitivity, *FF* is the flat-field correction for the VIRS arrays (FF=1 for the photomultipliers). S_I is light scattered out of position/pixel J by the grating and S_J' is light scattered into position/pixel J from all other wavelengths by the grating. Stray is the light at pixel/position J contributed by diffuse scatter from spectrometer internal structures. Ω is the instrument effective field of view (the responsivity averaged over the geometrical field of view divided by R_c). C_{Corr} is counts, which have been corrected for nonlinearity, dark signal, scattered and stray light, and normalized to unit flat field.

The signals from UVVS are counts from the photon-counting detectors, which depend weakly on temperature (See section 6.9). Their dark count background was determined by measuring the spectrum for 10-100 steps beyond the signal wavelength range. VIRS dark current was measured by periodically closing a shutter located at the entrance to the spectrograph. UVVS detector nonlinearity is caused by the processing dead time in the detector pulse-amplifier-discriminator and was corrected using equation 6.13. VIRS nonlinearity, which is caused by well saturation in the array detectors and by differential nonlinearity in the analog to digital converter, was negligible during calibration and will be negligible for signal levels incurred during flight observations.

Scattered light corrections include two terms. The first appears in the numerator and must be subtracted from observed signal (C) to correct for light scattered from all other wavelengths into position/pixel J: $S_I'(\lambda_j) = A \cdot \Delta\lambda \cdot FF_j \cdot \overline{\Omega} \cdot \int L(\lambda') \cdot R_c(\lambda') \cdot G(\lambda' - \lambda_j) d\lambda'$, where G is the instrument scatter function. The second term, which appears in the denominator and is proportional to the radiance at wavelength λ_J, represents the light scattered out of the bandpass. Stray light arises from diffuse scatter within the spectrometer (e.g. zero order wall scatter) the sum of stray+dark was estimated from portions of the spectrum where no real signal is present. (e.g. for wavelength positions below the atmospheric cutoff for UVVS or for wavelengths less than 230 nm for FEL lamp calibrations).

Responsivity is the quantum throughput (QT) of the optics and detectors at the center of the field of view and Ω is the effective field of view: $\overline{\Omega}(\lambda_j) = \int R(\lambda_j \theta, \phi) d\Omega / R_c(\lambda_j)$.

Radiometric calibrations using radiance standards (irradiance standards and reflectance screens) that fill the instrument aperture and field of view measure the quantity:

$$\overline{R} = A \cdot \Delta\lambda \cdot R_c(\lambda_j) \cdot FF_j \cdot \overline{\Omega} \qquad 6.9$$

Calibrations using standard detectors and star sources that fill only the aperture measure:

$$\overline{R}' = A \cdot R_c(\lambda_j) \cdot FF_j \qquad 6.10$$

Ω and $\Delta\lambda$ must be determined separately by scanning the field of view and measuring monochromatic lines respectively. Also, when a grating monochromator is used to scan a monochromatic source, C_{Corr}

in Equation 6.8, which represents the corrected counts observed at line center, is accurately determined by summing the corrected counts near line center and dividing by the ratio of instrument spectral bandpass to grating step size (Section 6.5.1).

6.8.1 UVVS

Figure 6.26 is a composite plot of UVVS radiometric sensitivity for continuous sources, as defined by Equation 6.9: $\overline{R} = A \cdot \Delta\lambda \cdot R_c(\lambda_j) \cdot FF_j \cdot \overline{\Omega}$. It is the result of measurements made using both the radiance and irradiance techniques described above. These values were measured at ambient temperature (~ 20° C) and must be slightly adjusted for the temperature dependence of the UVVS phtotmultipier detectors (Section 6.9.1).

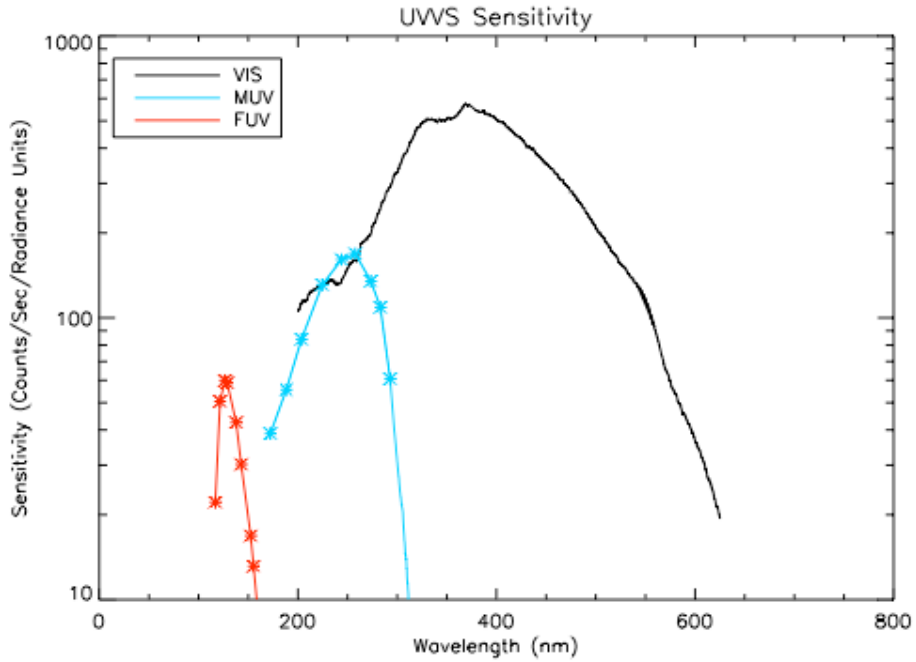

Figure 6.26 UVVS radiometric sensitivity for continuous spectral sources

For λ>200 nm, irradiance lamps were used to illuminate a white reflectance screen to produce a radiance source for the instrument. Both deuterium lamps (200<λ<400 nm) and FEL lamps (λ>280 nm) were used for these measurements. Responsitivity values derived from the deuterium and the FEL lamp agreed to better than 10% in their spectral overlap regions (280<λ<300 nm for MUV and 280<λ<400 nm for VIS). These measurements were made in cleanroom facilities at LASP and a spacecraft integration facility at the Applied Physics Laboratory. Calibration sequences included signal measurements, made when the lamps illuminated the screen, dark count measurements, made with the lamps on but the MASCS telescope aperture covered, and room-background measurements, made with a mask blocking the direct path from the lamps to the screen. These background measurements were subtracted from the normal calibration measurements to remove any contributions to screen radiance that were caused by secondary paths from the lamp to surfaces in the room to the scattering screen.

The radiance method requires accurate knowledge of the scattering screen properties and the atmospheric attenuation. Screen reflectance values were taken from manufacturer's data sheets for $\lambda>250$ nm. Relative reflectances for wavelengths $190<\lambda<300$ nm were measured by observing both the screen and the direct lamp with the MUV channel. These measurements were scaled to the published values for $\lambda>250$ nm to extend screen absolute reflectance to 200 nm. The atmospheric absorption coefficient was measured during each calibration by observing the screen at fixed distance and moving the lamp to measure the discrepancy between observed instrument output and the standard $1/R^2$ dependence. Corrections were applied for $\lambda<240$ nm using a path length that included the lamp-to-screen-to-instrument aperture distance plus over the 0.75 m traversed within the instrument.

Responsivity was calculated by correcting the observed counts for nonlinearity, dark count, and scattered light (flat field values equal 1 for scanning photomultipliers) and dividing by integration time and screen radiance corrected for atmospheric absorption. Nonlinearity corrections were calculated using Equation 6.13 (See Section 6.9.1). The sum of dark counts plus stray light was measured by scanning to wavelengths less than the atmospheric cutoff. Light scattered into wavelength λ from all wavelengths outside the bandpass (correction in the numerator of Equation 6.8) was calculated from the difference between the observed spectrum convolved with the instrument scattered light profile and to observed spectrum itself: $S_l^{'}(\lambda_j) \approx O(\lambda) \otimes G(\lambda) - O(\lambda)$ (Section 6.6). Light scattered out of the bandpass (correction in the denominator of Equation 6.8) was calculated from integrals of the scattered light profile over the appropriate wavelength intervals (Section 6.6).

Measurements made in the MOBI calibration facility were used to determine MUV responsivity for $\lambda<280$ nm and FUV responsivity for its entire wavelength range. MOBI produced a monochromatic irradiance source at the MASCS aperture. An auxiliary photomultipler detector, calibrated for absolute quantum efficiency against a NIST photodiode, was used to measure the absolute flux (photons per square cm per second) and uniformity of the beam illuminating the MASCS aperture. Dividing instrument corrected count rate, $C_{Corr}/\Delta t$, by the input beam irradiance measured by the auxiliary photomultiplier provided a direct measure of the product of the three instrument responsivity terms given by Equation 6.10. The procedures used to determine for the various corrections to C (excluding light scattered into the observed wavelength) were similar to those used for the scattering screen measurements. Values for Ω and $\Delta\lambda$,□□□□□ were required to convert between Equations 6.9 and 6.10, were taken from UVVS spectrometer field of view maps (Section 6.2.1) and calculated bandpass (Equation 6.6) using entrance and exit slit widths that were measured in the lab before instrument assembly. UVVS responsivity values calculated from the MOBI measurements are shown as symbols for 12 discrete wavelengths in Figure 6.26.

UVVS makes measurements of both continuous sources (surface reflectance and stellar calibration sources) and discrete sources (atmospheric line emission). For discrete sources the instrument bandpass is eliminated from the denominator of Equation 6.8 and:

$$L(\lambda_j) = \frac{[C(\lambda_j) \cdot N(C) - D(j) - S_l^{'}(\lambda_j) - Stray(\lambda_j)]/\Delta t}{A \cdot R_c(\lambda_j) \cdot FF_j \cdot \bar{\Omega} \cdot (1 - S_l)} = \frac{C_{Corr}(\lambda_j)/\Delta t}{A \cdot R_c(\lambda_j) \cdot \bar{\Omega}} \qquad 6.11$$

L is now the radiance (e.g. Watts per square cm per steradian) integrated over wavelength and C_{Corr} is the total corrected counts, summed over the emission line and divided by the ratio of banspass to step size. UVVS responsivity for lines sources is plotted in Figure 6.27.

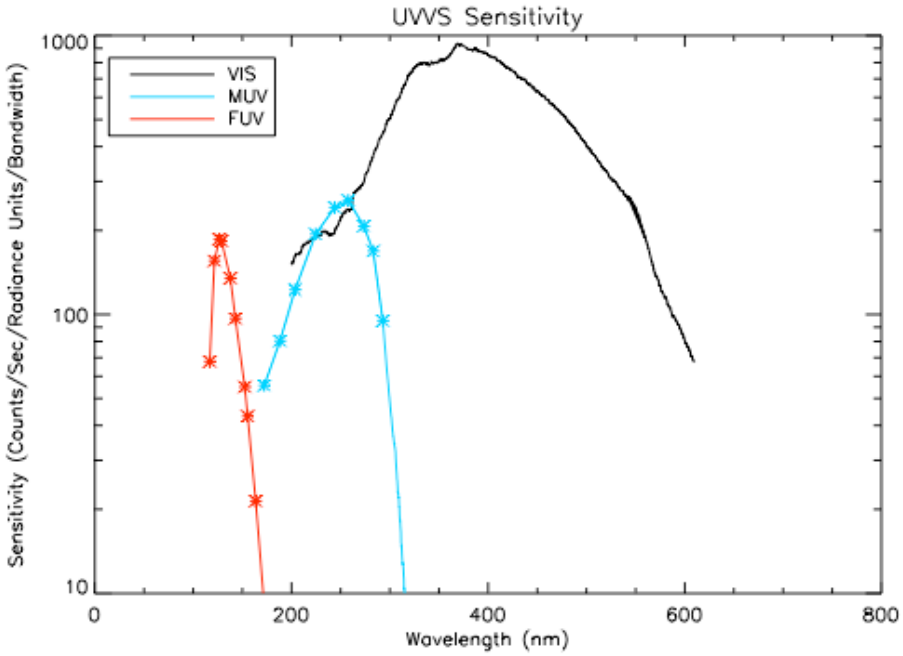

Figure 6.27 UVVS radiometric sensitivity for discrete spectral sources

6.8.2 VIRS

VIRS radiometric sensitivity for continuous sources is shown in Figure 6.28 in units of data number (DN) per radiance unit (Watts per square meter per steradian per micron). It was measured by observing a white reflectance screen that was illuminated by a NIST-calibrated FEL lamp F-540, located 50cm from the center of the screen along the normal. The MASCS telescope was pointed toward the center of the screen, at a viewing angle of 30º. These measurements were made in cleanroom facilities at LASP and a spacecraft integration facility at the Applied Physics Laboratory. Calibration sequences included signal measurements, made when the lamps illuminated the screen, dark count measurements, made with the lamps on but the MASCS telescope aperture covered, and room-background measurements, made with a mask blocking the direct path from the lamps to the screen. These background measurements were subtracted from the normal calibration measurements to remove any contributions to screen radiance that were caused by secondary paths from the lamp to surfaces in the room to the scattering screen. The instrument responsivity (Equation 6.9) was calculated by dividing the corrected instrument output DN (1 DN corresponds to 1190 electrons for both VIS and NIR detectors) by the screen radiance. Instrument output corrections include dark current, which was measured before and after each screen observation by closing the spectrograph shutter, and scattered and stray light, which were estimated using the procedure described in Section 6.6.2. Stray light, which was only significant for VIS wavelengths less than 350 nm, was determined from the average of DN values of pixels near

200 nm. Values shown in Figure 6.28 were measured at ambient temperature (~ 20˚ C) and must be slightly adjusted for the temperature dependence of the VIS detector (Section 6.9.2).

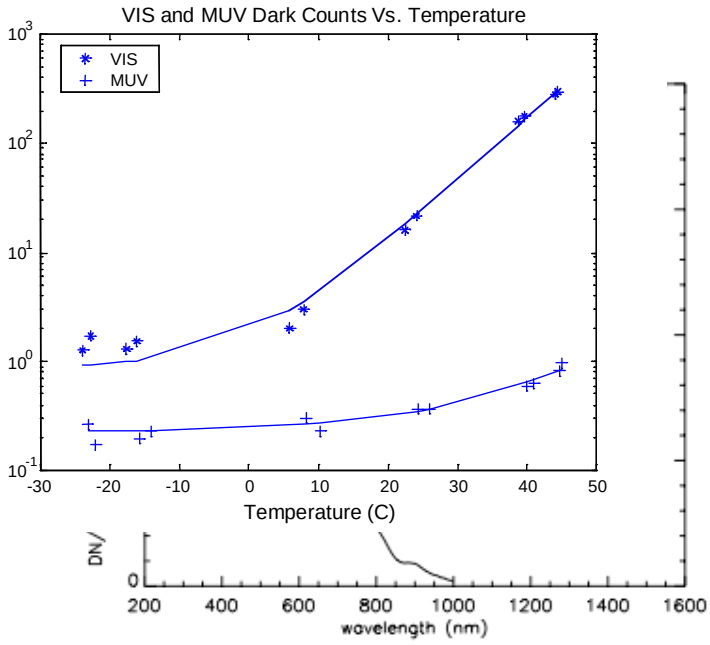

Figure 6.28 VIRS radiometric sensitivity for continuous spectral sources

6.9 DETECTOR CHARACTERISTICS

6.9.1 UVVS

6.9.1.1 Dark Counts

MASCS photomultiplier detectors produce 'dark counts' that arise from photocathode thermionic emission, which is a function of work function and temperature, and from radiogenic decay within their glass envelopes. The dark count temperature dependence was measured over a range from –23˚C to +45˚C in MOBI during thermal vacuum testing. Results for MUV and VIS are shown in Figure 6.29. These data were fit exponential functions yielding the following results, shown as solid lines fit to the data in Figure 6.29:

$$R(\mathrm{VIS}) = 0.9580 * \exp^{0.1294*T} + 0.8853$$
$$R(\mathrm{MUV}) = 0.01888 * \exp^{0.0778*T} + 0.2263 \qquad 6.12$$

It was not possible to fit an exponential function to the FUV dark count rate, which varied only slightly with temperature, changing from 0.1 counts per second at –25˚ C to 0.15 counts per second at +45˚ C.

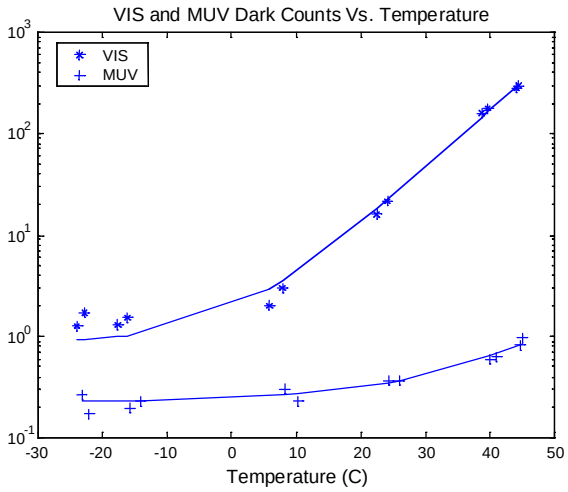

Figure 6.29 UVVS detector dark counts as a function of temperature

6.9.1.2 Linearity

The UVVS photomultipliers operate in pulse counting mode. Their outputs are coupled to Amptek A-111 pulse amplifier discriminators, which limit their pulse pair resolution (minimum resolvable time interval between two arriving pulses) to 120 nanoseconds. At high count rates, pulse pileup of the random photon arrival rate causes the output count rate to become nonlinear with the fraction of photons lost to the system equal to $C_O * \tau$, where C_O is the observed arrival rate (count rate), measured in Hz and τ is the pulse pair resolution, measured in seconds. In this case, true photon count rate is given by:

Thus an observed count rate of 5×10^5 Hz implies a true arrival rate of 5.3×10^5 Hz. Except for the Na D

$$C_T = \frac{C_O}{1 - \tau \bullet C_O} \qquad 6.13$$

lines at 589 nm, atmospheric emissions are expected to produce count rates less that 10^5 Hz resulting in a linearity correction negligible linearity correction. On the other hand surface observations with the UVVS can produce count rates greater that 5×10^5 Hz and it will be necessary to correct them for linearity before computing surface radiance.

6.9.1.3 Temperature Sensitivity

The UVVS radiometric sensitivity, which was reported in Section 6.8 for ambient temperature (~20˚ C), depends weakly on temperature. Figure 6.30 plots the temperature coefficient for UVVS detector sensitivity as a function of wavelength. Values for the FUV and MUV detectors are laboratory measurements of Hamamatsu photomultiplier tubes with Cesium Iodide and Cesium Telluride photocathodes respectively. VIS values were taken from data for a typical Bi-alkali phtotcathode, provided by Hamamatsu Photonics. All three detectors show a slight decrease in sensitivity with increasing temperature over most of their operating wavelength range with an abrupt increase at the longer wavelengths.

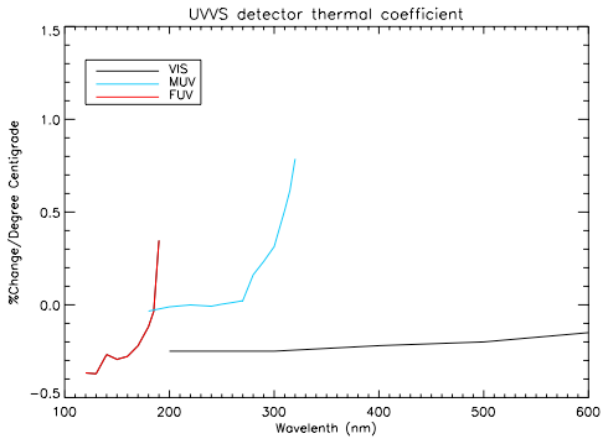

Figure 6.30 UVVS detector thermal coefficient

6.9.2 VIRS

Because neither detector will be actively cooled, the dark current must be routinely measured during both calibration and flight. Dark current characteristics for both VIS and NIR detectors were characterized as a function of temperature during thermal vacuum testing. These characteristics include dark current magnitude, dark current noise, and dark current pixel-to-pixel variation or dark current flat field (to be distinguished from the signal flat field, which is pixel-to-pixel variation observed for uniform illumination by photons and excluding dark current.

6.9.2.1 Dark Current Magnitude and Pixel-to-pixel Nonuniformity

Figure 6.31 shows representative plots of detector dark fields for detector temperatures in the range –10˚ C to + 8˚ C, which include both dark current and a detector-specific offset (1050 DN for VIS and 2175 DN for NIR) that are included to ensure no values are lost outside the digitization range. Over this temperature range, the VIS detector dark charge magnitude (~1125 DN) and pixel-to-pixel nonuniformity (~±15 DN peak to peak, ~ 7 DN rms) are relative unchanged. On the other hand, the NIR dark charge changes by 50% and there is a factor of 4 increase in pixel nonuniformity. The temperature dependence for average dark current magnitude and rms pixel-to-pixel variation is summarized in Figure 6.32, where symbols in the left and right panels show the average dark charge and rms deviation measured with a 1 second integration time at 6 thermal vacuum dwell temperatures. The solid lines in the left panel are exponential curves of the form $y = a_0 a_1^{\,T} + a_2$ fit to the average dark values yielding values a_0=48.4, a_1=1.13, a_2=1045.8 and a_0=2673, a_1=1.067, a_2=2181.9 for VIS and NIR respectively. NIR dark current nonuniformity (pixel-to-pixel variations in the dark current) increases rapidly with increasing temperature, changing from 100 DN at –11˚ C to 2000 DN at +16˚ C.

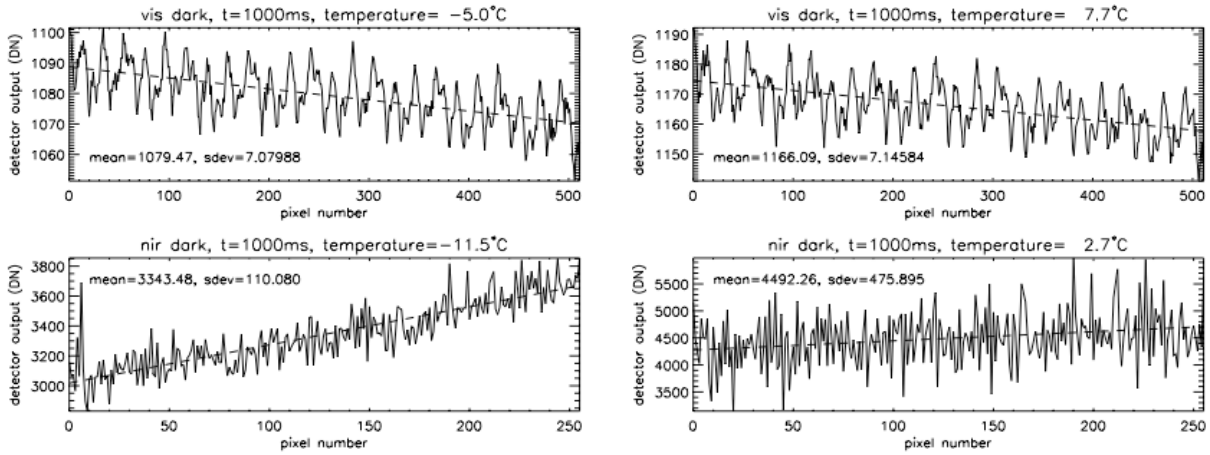

Figure 6.31 Examples of VIRS detector dark current

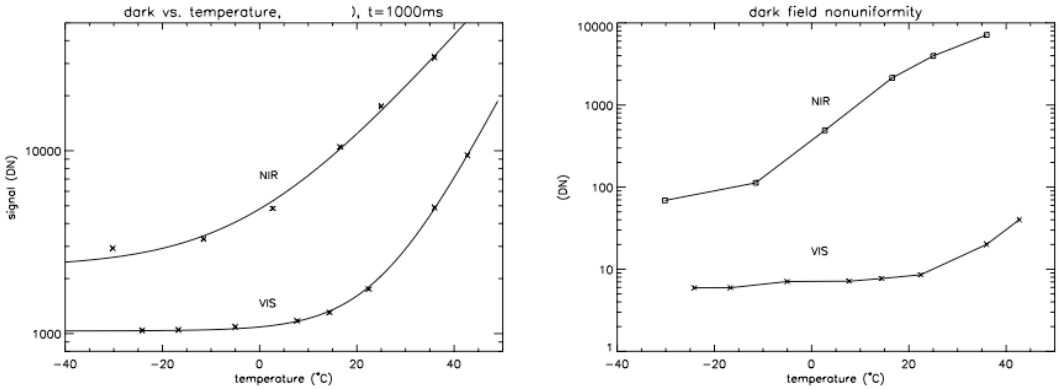

Figure 6.32 VIRS detector dark current and dark field nonuniformity as a function of temperature

6.9.2.2 Dark Current Noise

The thermal characteristics of VIRS detector dark current noise were measured during thermal vacuum testing. In the absence of input photons, the two significant noise sources for the VIRS detectors are read noise and dark current noise, which sum in quadrature. Average total detector noise (read noise and dark noise) was calculated at each temperature from a series of contiguous dark frames, which were acquired using 1.0-second integration times. The mean and standard deviation was calculated for each pixel, treating it as an independent detector. These individual standard deviations were averaged to determine a single average value for the array. The measured noise levels are shown in Figure 6.33 for both VIS and NIR detectors as 'x's. Read noise values, which were estimated from the values at the coldest temperatures, when the dark current is negligible, are 4.5 DN (5350 electrons) and 7.3 DN (7500 electrons) for VIS and NIR, respectively.

For an ideal solid state detector, the dark noise is the result of dark current shot noise, which is simply the square root of the number of electrons accumulated as dark charge during an integration time and

can be calculated from the values reported in the left panel of Figure 6.32 as follows. The number of electrons collected during an integration is 1190*DN, where 1190 electrons per DN is the detector gain for the VIRS detectors. The rms noise (electrons) is the square root of 1190*DN and the rms noise (DN) is the square root of DN divided by square root of 1190:

$$\Delta e = \sqrt{1190 \cdot DN} \text{ and } \Delta DN = \sqrt{DN} / 34.5$$

For example, the NIR dark at 16˚ C is 7825 DN (10^4 – 2175 offset) and the dark current shot noise is 2.6 DN.

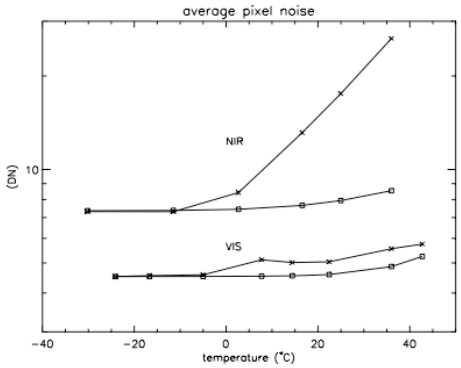

Figure 6.33 VIRS dark current noise as a function of temperature 'X' are the observed values. Squares are estimates based on the quadrature sum of read noise and dark current shot noise.

Squares in Figure 6.33 show the ideal detector dark noise, calculated from the quadrature combination of the read noise and dark current shot noise. For the VIS detector, the observed dark noise is only slightly larger than the ideal case. On the other hand, the observed NIR dark noise shows a significant departure from the ideal case for temperatures greater than 0˚ C. This behavior suggests that NIR observations during operations should be scheduled for times when the NIR detector temperature is ≤ 10˚ C whenever possible in order to hold detector noise to ~ 10 DN or less. Figure 6.34 shows predicted MASCS maximum and minimum component temperatures versus Mercury true anomaly, suggesting that segments of orbits close to the planet should be avoided for seasons in for which the planet true anomaly is in the range 260˚ to 350˚.

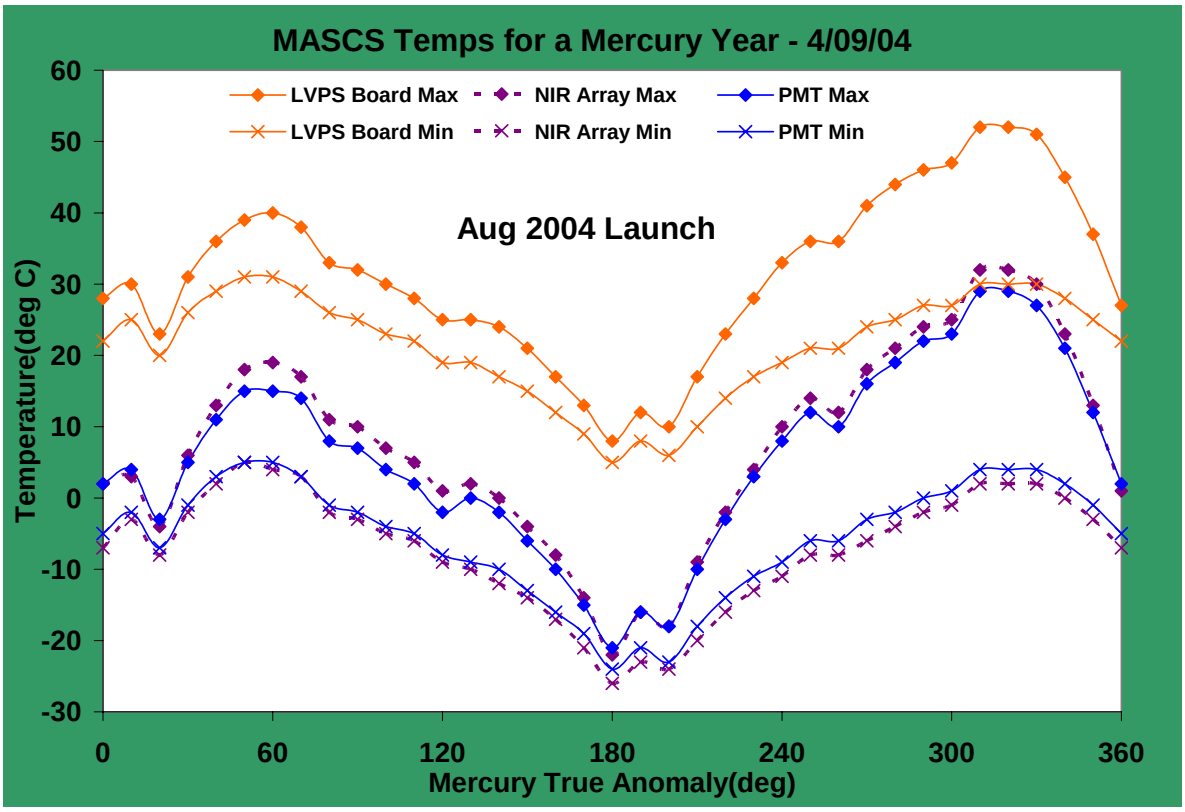

Figure 6.34 Predicted MASCS component temperatures during one Mercury year

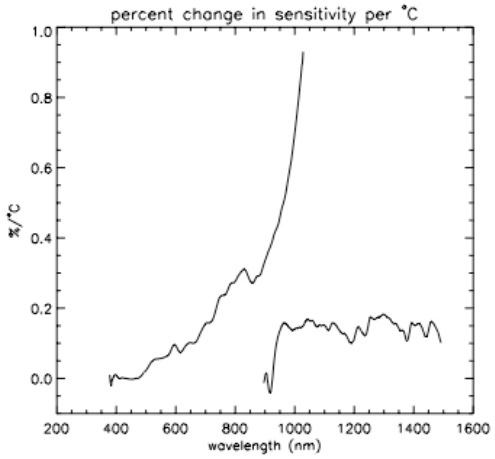

Figure 6.35 VIRS detector temperature coefficient

6.9.2.3 Temperature Sensitivity

The VIRS radiometric sensitivity, which was reported in Section 6.8 for ambient temperature (~20˚ C), depends weakly on temperature. Figure 6.35 plots the temperature coefficient for VIRS detector sensitivities as a function of wavelength, which were measured during thermal vacuum testing by observing a stable quartz halogen lamp located outside the vacuum enclosure. These curves show the

average change in sensitivity over the range –21˚ C to +44˚ C. The NIR temperature coefficient is essentially wavelength independent at ~ 0.15% /˚C. On the other hand, the VIS coefficient increases as a function of wavelength from 0 at 400 nm to ~ 0.9%/ºC at 1micron. This behavior is typical of silicon solid state detectors.

7.0 DATA PRODUCTS

The MASCS team will deliver the following calibration data products to the MESSENER Science Operations Center:

1. Raw instrument data used for instrument characterization and calibration as well as the ancillary data required for interpreting the instrument data to infer calibration parameters. (e.g. lamp irradiance values as a function of wavelength, lamp-to-screen and screen-to-instrument geometry used for the radiometric sensitivity, and standard photomultiplier tube calibration and MOBI beam maps used to determine UVVS radiometric sensitivity in the vacuum ultraviolet)
2. Algorithms and instrument parameters required by the SOC to produce radiance values for a specified target (surface latitude and longitude or atmosphere tangent point latitude and longitude as well as altitude above the surface) as a function of wavelength from the telemetered instrument data. These include wavelength scale, UVVS bandpass, instrument geometric parameters required to retrieve radiometric sensitivity, pointing offsets, and temperature dependences.
3. Tables of instrument characteristics for inclusion in the SOC database. These include field-of-view maps, telescope off-axis response, spectrometer scattered light, spectrometer polarization, radiometric sensitivity as a function of wavelength, detector sensitivity as a function of temperature, and detector dark output as a function of temperature.

8.0 REFERENCES

Adams, J., and McCord, T.M. (1970) Remote sensing of lunar mineralogy: Implications from visible and near-infrared reflectivity of Apollo 11 samples. Proc. Apollo 11 Lunar Sci. Conf., 1937-1945.

Binda, T. A., Killen. R. M., and Morgan, T. H. (2000) Discovery of Calcium in Mercury's Atmosphere. Nature, **404**: 159-161.

Blewett, D.T., Lucey, P.G., Hawke, B.R., Ling, G.G., and Robinson, M.S. (1997) A comparison of Mercurian reflectance and spectral quantities with those of the Moon, Icarus **129**, 217-231.

Blewett, D.T., Lucey, P.G., Hawke, B.R. (2002) Lunar pure anorthosite as spectral analog for Mercury, Meteoritics & Planetary Science **37**, 1245-1254.

Broadfoot,A. L., Kumar, S., Belton, M.J.S., and MaElory, M.B. (1974) Mercury's Atmosphere from Mariner 10: Preliminary results. Science **185**: 166-169.

Broadfoot, A. L., Shemansky, D. E., and Kumar, S. (1974) Mariner 10: Mercury Atmosphere. Geophys. Res. Lett. **3:** 577-580.

Burbine, T.H., Mccoy, T.J. , Nittler, L.R., Benedix, G.K., Cloutis E.A., and Dickinson, T.L. (2002) Spectra of extremely reduced assemblages: Implications for Mercury, Meteoritics & Planetary Science **37**, 1233–1244.

Butler, B. J., Muhleman, D. O., and Slade, M. A. (1993) Mercury: Full-Disk Radar Images and the Detection and Stability of Ice at the North Pole, Journ. Geophys. Res. **98**, 15003-15023.

Hord, C.W., W.E. McClintock, C.A. Barth, L.W. Esposito, A.I.F. Stewart, G.E. Thomas, B.R. Sandel, D.M. Hunten, A.L. Broadfoot, D.E. Shemansky, J.M. Ajello, A.L. Lane, and R.W. West, Galileo Ultraviolet Spectrometer Experiment, Space Sci, Rev, **60**:503-530, 1992.

Hunten, D. M., Morgan, T. H., and Schemansky, D. E. (1988) The Mercury Atmosphere, in Mercury, Vilas, Chapman, and Mathews eds, University of Arizona Press, 562-612.

Killen, R. M., Potter, A. E., and Morgan, T. H. (1990) Spatial Distribution of Sodium Vapor in the Atmosphere of Mercury, Icarus, **85**, 145-167.

Killen R. M., Benkoff, J., and Morgan T. H. (1997) Mercury's Polar Caps and the Generation of an OH Exosphere, Icarus, **125**, 195-211.

Lucey, P.G., Blewett, D., and Hawke, B. (1998) Mapping the FeO and TiO2 content of the lunar surface with multispectral imagery, J. Geophys. Res. **103**, 3679-3699.

Lucey, P.G., Blewett, D.T., and Jolliff, B.L., (2000a) Lunar iron and titanium abundance algorithms based on final processing of Clementine ultraviolet-visible images, Geophys. Res., **105**, 20,297.

Lucey, P.G., Blewett, D.T., Taylor G.J., and Hawke, B.R. (2000b) Imaging the maturity of the lunar surface, J. Geophys. Res, 1**05**, E8, 20297-20305.

Lucey, P.G. (2004) Mineral maps of the Moon, Geophys. Res. Letts. **31** 10.1029/ 2003GL019406.

Maymon, S.W., Neeck, S.P., and Moody, J. C. Sr., Optical design alternatives for the Moderate-Resolution Imaging Spectrometer for the Earth Orbiting System, **S**ociety of Photo-Optical Instrumentation Engineers, **924:**10-22,1988.

McGrath, M. A. , Johnson, R. E., and Lanzerotti, L. J. (1986) Sputtering of Sodium on the Planet Merucry, Nature, **323**, 694-696.

Mendillo M., Baumgardner, J., and Flynn, B. (1991) Imaging Observations of the Extended Sodium Atmosphere of the Moon, Geophys. Res. Lett, **18**, 2097-2100.

Morgan, T. H., and Killen, R. M. (1996) A Non-Stoichiometric Model of the Composition of the Atmospheres of Mercury and the Moon, Planteary and Space Science, **45**, 81-94.

Potter, A. E. and Morgan, T. H. (1985) Discovery of Sodium in the Atmosphere of Mercury, Science **229**, 651-653.

Potter, A. E. and Morgan, T. H. (1986) Potassium in the Atmosphere of Merucry, Icarus, **67,** 336-340.

Rava, B., and Hapke, B. (1987) An analysis of the Mariner 10 Color Ratio Map of Mercury, Icarus **71**, 397-429, .

Robinson, M.S. and Lucey, P.G. (1997) Recalibrated Mariner 10 color mosaics: Implications for mercurian volcanism, Science, **275**, 197-200.

Robinson, M.S., and Taylor, G.J. (2001) Ferrous oxide in Mercury's crust and mantle, Meteorit. Planet. Sci. **36**, 841-847.

Slade, M. A., Butler, B. J., and Muhleman, D. O., (1992) Mercury Radar Imaging: Evidence for Polar Ice, Science, **258**, 635-640.

Sprague, A. L. (1990) A Diffusion Source for Sodium and Potassium in the Atomspheres of Mercury and the Moon, Icarus, **84**, 93-105.

Sprague, A. L., Hunten, D. M., and Lodders, K. (1995) Sulfur at Merucry, Elemental at the Poles aand Sulfides in the Regolith, Icarus, **118**, 211-215.

Sprague, A. L., Kozlowski, R. W. H., Hunten, D. H., and Grosse, F. A. (1993) An Upper Limit on Neutral Calcium in Mercury's Atmosphere, Icarus, **104,** 33-37.

Sprague, A.L., Emery, J.P., Donaldson, K.L., Russell, R.W., Lynch, D.K., and Mazuk, A.L. (2002) Mercury: mid-infrared (3-13.5 mm) observations show heterogeneous composition, presence of intermediate and basic soil types, and pyroxene, Meteorit. Planet.Sci**.** **37**, 1255-1268.

Vilas, F. Mercury: Absence of crystalline Fe2+ in the regolith, Icarus **64**, 133-138, 1985.

FSCM NO.	SIZE	DRAWING NO.	REV.
88898	A	7384-9470	A
SCALE	DO NOT SCALE PRINT	SHEET 49 of 49	